University of Twente
Bachelor thesis Electrical Engineering

COMSOL Multiphysics modeling of acoustic actuation in a microfluidic, mass-transporting reactor

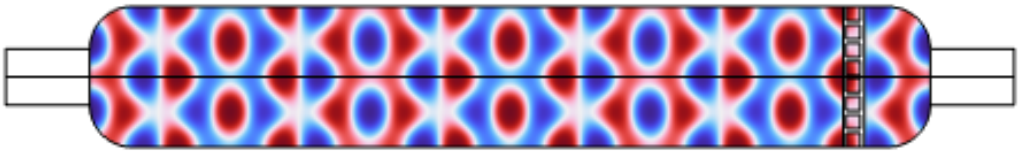

Fig. 1: Acoustic pressure plot at 3.7025 [MHz]

H.F. Twerda
s2837242

M. Odijk
Committee chair - Professor IDS

S. Le Gac
External committee member - Professor AMBER

July 6, 2025

CONTENTS

I. Abstract

***Abstract*—This study investigates the influence of ultrasonic actuation on fluid dynamics and mass transport within microfluidic channels using COMSOL Multiphysics simulations. The purpose behind these simulations is to investigate if and how ultrasonic actuation can be used to improve the weathering of Olvine for CO_2 capture. Microfluidic systems, such as lab-on-a-chip devices, offer promising development avenues for biomedical and chemical analysis because of their compact size and precise control of microscale flows. Ultrasonic or acoustic actuation has been identified as an attractive tool for enhanced mixing, pumping, and particle manipulation. This work models the effects of high-frequency acoustic actuation on micrometer-scale fluid channels and analyzes the resulting changes in flow patterns and mass transport. The study identifies key insights on frequency choice and node placement and attempts to show that acoustic actuation significantly impacts the balance between convection and diffusion in mass transport.**

II. Introduction

Human activities have been climate change's major driver in the 21st century [1]. Global warming through the output of greenhouse gasses has caused the global surface temperature to rise by 1.1 degrees Celsius compared to preindustrial temperature levels. More extreme weather phenomena have been observed throughout the last decade, affecting much of the human population. These extreme weather events cause food and water insecurity, ecosystem damage, a disease-susceptible environment, and many other potential crises [1]. Various solutions have been or are currently being developed to combat these greenhouse gas emissions of the past, present, and future. One of the more known greenhouse gasses is CO_2. It is by far the most common greenhouse gas and it is estimated to comprise approximately 80% of the greenhouse gasses mix (79.7% in 2022 in the United States of America [2] and 80.6% in 2024 in the European Union [3]). This study will focus on CO_2. There are two main approaches to reducing the greenhouse gas (GHG) problem. One is through reducing emissions outputted to the atmosphere. This can be done either through a reduction of comsumption or through innovations that reduce the output of GHG's of the goods and/or services. The other method to address the problem of GHG emissions is by reducing the GHG emissions that are already present in the air. This is what is often referred to as carbon sequestration. Carbon sequestration focuses on capturing and storing CO_2 in the earth, flora, and through reaction products with rocks for a longer period [4] [5]. Trees are the most commonly known form of CO_2 sequestration. This also means that carbon sequestration is natural and man-made [4]. Other forms of carbon sequestration can be through direct air capture, other vegetation, and through (ultra-mafic/mafic) rocks. Research at the BIOS group in close collaboration with spin-off company Paebbl focusses on carbon sequestration [6] [7]. Currently, CO_2 is emitted through various actors, one of the largest being the concrete industry. They are estimated to emit around 8% of the world's emissions [8] [9]. To reduce the carbon footprint of the process, some organizations have started to capture the CO_2 from the emission process. Although this is a step in the right direction, it is not a full-circle solution. A way to use the captured carbon is by sequestering the CO_2 through carbonation with ultra-mafic and mafic rocks [10]. Mafic rocks are a subset of igneous rocks that are formed by cooling molten earth material. These mafic rocks are generally high in sillicates such as olivine. olivine is used as a CO_2 sequestration method. It can be used in a natural setting (e.g., on beaches) and in a stirring setup with liquid CO_2 to enhance the reaction between CO_2 and olivine [10]. However, the current process is heavy-wearing in which stirring materials and containers frequently require replacement and the reaction process is relatively slow [11]. A high potential method to improve understanding of the reaction process is the development of microreactors in Lab-on-a-Chip (LoC) devices. LoC devices facilitate the testing of a wide range of experimental options. The pressure can be increased, the flowrate can be adjusted, the temperature can be fluctuated and external tools such as lasers or ultrasonic waves can be used to influence the microenvironment [12]. Moreover, LoC's are compact, accurate, and allow for low cost protoyping [12]. Kleinsmit developed such a microreactor in an LoC device that allows the reaction between olivine particles and CO_2 to occur at a high temperature and under high pressure conditions [7]. The preliminary results indicated a significant initial reaction rate. However, this slowed down at a later stage, which is hypothesized to happen due to the formation of passivation layers on the partially reacted olivine particles [7]. Ultrasound was suggested as an avenue for development to address these passivation layers around olivine particles. Hence, the research goal of this study is to investigate the response of an ultrasonic wave applied to the LoC microreactor of Kleinsmit using the COMSOL Multiphysics simulation tool.

III. Literature review

A. CO_2 sequestration through mineral carbonation

Mineral storage of CO_2 seems to be one of the most permanent solutions to the modern day climate change problem [13]. The longevity of this storage, compared to other forms of carbon storage such as through vegetation and soils, is incomparable. Mineral rocks can store CO_2 for millions of years, where vegitation and soils are limited to decades, centuries, or millenia. The storage potential of these mineral rocks is nearly infinite and potentially valuable by-products can be created through reactions with CO_2 [13]. However, the natural process of mineral carbonation is not fast enough to keep up with or compensate for the emissions of yesterday, today, and tomorrow. To have a chance of reaching the climate goals set up by an organisation such as the European Union, several challenges of mineral carbonation need to be addressed. Among these are; the slow mineral-fluid interaction, the impact of mining required to excavate these materials, in some cases energy-intesive pretreatment, the high energy costs required to hasten the reaction kinetics and the overall economic viability of mineral carbonation [13] [14] [15]. These are challenges that have to be solved in order for mineral carbonation to be seen as an appropriate and effective, partial, solution to

climate change. The world "partial" is stressed here as CO_2 sequestration should not take away from the effort to reduce emissions. CO_2 sequestration should focus on the alleviating the effects that are currently present and aid the sectors that find difficulty in transforming towards CO_2 neutrality. There are differences between the methods of mineral carbonation. Olajire makes a distinction between three different archetypes of mineral carbonation. In-situ, ex-situ, and other forms [13] [14] [15]. In-situ mineral the original place, and in the case of mineral carbonation this is generally underground. The carbon is injected underground and the environmental conditions are optimised to facilitate the natural reaction process. Ex-situ is the more commonly known idea within mineral carbonation technologies (MCT's) and refers to the process of treating the CO_2-mineral reaction in an industrial process setting [13] [14] [15]. The heading "other" is used by Olajire for two different MCT's; passive and biomineralisation [15]. Passive refers to the natural process of mineral carbonation [15]. Biomineralisation refers to the use of living organisms to aid in precipitation processes. It should not be seen as an alternative to the geological storage of carbon but rather as a solution in specific scenarios [15]. One of the materials proposed for mineral carbonation is olivine. olivine, consisting out of the chemical mix of magnesium iron sillicate, is one of the most common minerals on earth. olivines can be found in ultramafic and mafic igneous rocks and are abudently found in the earth's rock mantle. Its abundance is one of the advantages in the considerations for CO_2 sequestration. Its chemical formula is $(Mg, Fe)_2SiO_4$. The reactivity between olivine and CO_2 has been demonstrated in the literature [16]. Garcia et al. found in their experiments with supercritical CO_2 (150 C°) and 150 bar) that $57\% \pm 2\%$ of the CO_2 was sequestered, with its main reaction product being magnesite and amorphous silica in low concerations[16]. Olivine has been suggested as a method for CO_2 sequestration in various papers. Several of those papers describe the uses of olivine in coastal zones [17] [18] [19]. These tropical zones would induce increased weathering which would speed up the reaction between olivine and CO_2. Similar approaches have been proposed for olivine in combination with coastal locations. The increased alkilinity in the water would increase the CO_2 uptake from sea-air interaction. However, more reseach is required to estimate the risks and costs paired with introducing olivine to the sea. These include ecological effects, economical viability, (potential) secondary reactions and dissolution reactivity [18] [19]. Bearat et al. have shown that the reaction between olivine and CO_2 produces a reaction-inhibiting layer that is largely composed of silica [20]. This is more generally known as a passivation layer and has been observed in several papers on the mineral carbonation of olivine [20] [10] [21]. The passivation layers of olivine inhibit the reaction between the CO_2 and olivine particles which causes the reaction to slow down.

B. Acoustic cavitation

One of the proposed options to break these passivation layers in olivine and thus assist the carbonation process of olivine is through acoustic cavitation. Ultrasound-intensified carbon sequestration makes use of frequencies above the human hearing range (>20kHz) to cavitate microbubbles that are actuated (through resonance) by ultrasonic waves. The process of acoustic cavitation makes use of microbubbles in water that are actuated by ultrasonic waves. These microbubbles expand and shrink in size due to linear or non-linear resonance [22]. The bubble pulsates and takes on a large range of bubble radii. It can violently collapse if the acoustic amplitude is significant enough to incite strong pulsations [22]. This phenomenon occurs on the premise that the chosen bubble radius matches the range of bubble radii required for resonance at the chosen acoustic amplitude. A different experiment with acoustics was done in the paper of Segers & Versluis on acoustic bubble sorting for ultrasound contrast agent enrichment [23]. In their paper, Segers & Versluis provide a bubble sorting theory that uses ultrasound as its sorting method through bubble resonance. They added an ultrasound piezo perpendicular to their LoC flow setup to elevate the y-level of resonating bubbles. Segers & Versluis recommended a traveling wave due to its wavelength being independent of channel dimensions, thus allowing optimization without altering the chip design [23]. Traveling waves work for chips with low reflectivity. For high reflectivity chips, a standing wave is needed within the channel. A visualization of the effects of ultrasonic-induced cavitation is important to understand how ultrasonic-induced cavitation can enhance the mineral carbonation process. This is shown in Wagterveld et al.'s paper, where they used acoustic cavitation on suspended calcite crystals intending to visualize the acoustic cavitation effects [24]. Wagterveld et al. differentiate between cluster and stream cavitation. Cluster cavitation refers to the formation and clustering of cavitation bubbles, that then collapse together, generating a strong local impulse. Wagterveld et al. observed that the force generated by these cluster cavitations was able to cause three different forms of impact; attrition, disruption of aggregates, and deagglomeration [24]. The second form of cavitation bubbles encountered by Wagterveld et al. was streamer cavitation. This refers to the formation and clustering of cavitation bubbles in the form of strings. The collapse of this string releases localized impulses across a larger surface area and hence generates less impact on one place in the volume (as compared to cluster cavitation). Due to its decrease in localized impact, streamer cavitations were found to only cause deagglomeration [24]. Another finding of Wagterveld et al. was regarding circular indentations in the formed calcite when they investigated it with a scanning electron microscope (SEM). Wagterveld et al. argued that this was likely due to shockwave-induced jet impingements (high-velocity fluids directed at a surface) [24]. Wagterveld et al.'s article on visualizing the effects of acoustic cavitation on minerals provides a hopeful outlook on removing or decaying the passivation

layer on olivine. Acoustic cavitation has been proposed and used for applications in fields such as surface finishing, agri-food, non-invasive medical monitoring, pathogen deactivation, and drug delivery [25] [26] [27] [28]. Another research area for acoustic cavitation is the field of mineral carbonation. Santos et al. investigated how ultrasound can aid the process of mineral carbonation [11]. The aim was to use stainless steel slags to sequester CO_2 and reduce their alkalinity. The study evaluated the differences between mechanical mixing and mechanical mixing assisted by an ultrasound probe. The evaluations also showed a difference in the results due to the positioning of the ultrasound. These experiments were carried out at intervals of four hours and at a consistent temperature of 50 degrees Celsius [11]. The results showed that a continuous ultrasound-intensified mixing process improved the reaction the most. The periodic ultrasound-intensified mixing process also showed improvements compared to the baseline of pure mechanical mixing. However, the economic aspect in terms of energy costs was an important limitation of the study. Santos et al. determined that with the energy costs and the energy mix at that time, it was not feasible to capture more CO_2 than was emitted through the ultrasound-intensified process [11]. A new avenue for this could be the use of green energy to reduce the carbon consumption of the process [11]. So far, the process of using ultrasonic cavitation to decay the passivation layer of olivine has not yet been visualized in detail. A gap in the literature remains as to how ultrasound impacts Olvine particles in a LoC environment and how ultrasonic actuation can be used to improve the concentration profile of mass transport in LoC devices.

C. The Bachelor of Science assignment

Throughout this review of the literature, it has become evident that tackling the olivine passivation layer could bring great benefits when it is used later for CO_2 sequestration [10]. Ultrasound is one of the promising options for the decay of the passivation layer of olivine, as has been demonstrated in other similar cases [11] [24]. Santos et al. [11] have shown that ultrasonic acoustic actuation appears to improve the reaction rate; however, this process has not yet been visualized and has not been done on olivine particles. Wagterveld et al. [24] show the potential effects of acoustic cavitation and actuation (its standalone effect) using suspended calcites crystals, and this provides a hopeful outlook for the effects of ultrasonic actuation on the passivation layer of olivine. The introduction to bubble resonance theory given in the article by Segers & Versluis provides valuable information as to how to design such a set-up [23]. The main differences lie in the applications (mixing vs. sorting) and the materials inside the LoC environment (liquid and olivine particles vs. pure liquid). The hypothesis is that the ultrasonic actuation can induce significant improvements in the decay of the passivation layers of the olivine particles in the LoC device. A COMSOL Multiphysics simulation model is designed to investigate the effects of acoustic actuation within a microfluidic mass transporting channel. In summary, the purpose of this study is to investigate how ultrasound and its acoustic actuation properties can be simulated in a microfluidic chip channel using the COMSOL Multiphysics tool. This study will focus on designing a simulation that integrates three different physics phenomena; fluid flow, mass transport, and acoustics. The main research question is as follows:

- How does acoustic actuation affect fluid flow and mass transport in microfluidic channels, based on insights gained from simulation using COMSOL Multiphysics?

This study hypothesizes that ultrasonic actuation induces acoustic pressure gradients that significantly influence fluid flow and mass transport within microfluidic channels. The extent of this influence is expected to scale with the magnitude of the applied voltage, as higher voltages generate greater acoustic pressures, leading to stronger fluid perturbations and enhanced mass transport effects.

IV. Methodology

This section describes the design choices and methods that were used in the study. It discusses frequency calculations, 2D design specifications and COMSOL Multiphysics considerations.

A. Frequency Calculation

The frequency calculation for the piezoceramic resonator depends on the material of the chip and the material of the piezoceramic resonator. The Master of Science thesis of L. Kleinsmit describes microfluidic chips made of glass-sillicon [7]. These chips use a mixture of water and CO_2 in their flow. The choice of chip material influences how acoustic waves can be used on the chip. For glass-silicon, the reflection coefficient of glass-silicon is high and thus allows (almost) no traveling waves to go through the glass interface. To allow ultrasound to enter the channel, standing waves should be generated in the channel. This can be done by vibrating the chip with a piezoceramic resonator. The deciding factor in choosing the operating frequency for a standing wave is the width of the channel. The chosen design (Constant Temperature microreactor, see section VIII-C) uses a 1mm wide channel in the reactor room. For a standing wave to form in the channel, its wavelength should be at most twice the size of its width. The conversion of wavelength to frequency using eq. (1) provides a frequency of approximately 740 [kHz] for a single standing wave to form in the channel considering a medium of water at 20 degrees Celsius (c = 1481 [m/s]). Similarly, for a 0.5 [mm] channel width, the resonance frequency doubles to approximately 1.48 [MHz]. For liquid CO_2 at 20 °Celcius (and 5.7291 [MPa]) the speed of sound is 337.65 [m/s] [29]. Following eq. (1), this leads to a frequency of approximately 169 kHz. The mixture of CO_2 and water (H_2O) changes the speed of sound based on the composition of the mixture, the applied pressure, and the temperature. Each piezoceramic resonator can be driven on a range of frequencies surrounding its resonance frequency. The standing waves generated will have two antinodes, at the edges of the channel, and one node in the middle of the channel (see fig. 2).

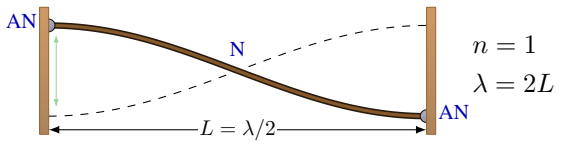

Fig. 2: Standing wave, double free

The resonance frequency of a bulk square piezoceramic resonator is calculated through its respective dimensions. A bulk resonator generates its resonance frequency through deformation of the piezoceramic material. The formula for calculating the frequency of a wave is as follows:

$$f = \frac{c}{\lambda} \tag{1}$$

Here, c is the speed of sound in the medium, λ is the wavelength of the acoustic wave, and f is the frequency that belongs to the combination of a particular speed of sound and wavelength. The resonance frequency of a wave is based on the constructive interference of waves. For resonance to occur, the phase of a round-trip wave has to equal the phase of a starting wave. When not aligned, the summation of the two waves results in a suboptimal output compared to the resonance frequency production. The resonance frequencies of a square resonator can be calculated by integrating the phenomenon described above into eq. (1). Moreover, λ should fit the dimension of the resonator (d) [30]. For a round-trip, a value of 2d is the minimal value for resonance. The minimal resonance value (2d) is called the fundamental frequency. Any positive number can expand this to find higher harmonics, as can be seen in the formula below:

$$f_r = \frac{Nc}{2d} \tag{2}$$

Here, N is any positive integer number and d is the length of any side of a square resonator. A similar calculation can be made for a circular piezoceramic resonator, taking into account the spherical symmetry. To calculate the measurements for the required piezoceramic resonators, the formula is rewritten as follows:

$$d = \frac{Nc}{2f_r} \tag{3}$$

In piezoceramic material (lead zirconium titanate, PZT), the propagation speed of the wave is between 3500 [m/s] and 4500 [m/s] [31]. The value of c used in the calculations is 4000 [m/s]. The thickness of the 740 [kHz] resonator thus becomes approximately 2.7 [mm]. The height and width also provide resonance frequencies. For practical purposes, these values can be chosen as 5 [mm] (with an estimated resonance frequency of 400 [kHz]). This is to prevent the resonance frequencies from overlapping and causing potential destructive interference.

B. 2D Design

The two dimensional (2D) design in COMSOL Multiphysics is shown in fig. 3. The main reason for building a 2D model instead of a 3D model was to reduce the simulation time. 3D simulations are significantly more complex and require longer simulation times. A 2D model was built to reduce complexity and accommodate time constraints. The 2D model is designed to be symmetric with the x-axis in all three physics domains. This symmetry across domains allows for only simulating half of the reactor channel. The mirror 2D data set together with the appropriate boundary conditions in each domain should yield equal results as the full simulation in 2D. The creeping flow is symmetric on the x-axis. For the transport of diluted species, the concentration component has to come from the upper inlet to be symmetric across the x-axis. The pressure acoustics, frequency domain module models acoustic pressures and waves. The wave is modeled as a moving wall that generates a standing wave within the channel in the y-direction.

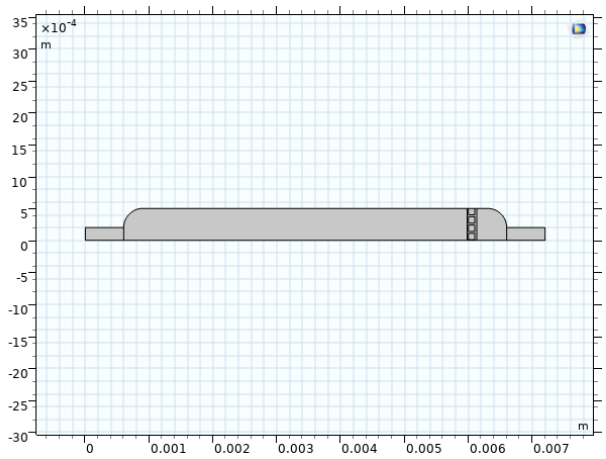

Fig. 3: 2D model microfluidic reactor, symmetric across x-axis

C. COMSOL Multphysics Considerations

Each physics module in COMSOL requires its own settings and boundary conditions to yield a functional and realistic model. First, the separate modules, their settings, and their boundary conditions are discussed. This is followed up by the multiphysics considerations and combined they form the complete model.

1) Creeping flow module: The creeping flow module is created by neglecting the inertial component in the Navier-Stokes equations of the laminar flow module [32] [33] [34]. The main reason for neglecting the inertial component of the Navier-Stokes equations is a Reynolds number that is (much) smaller than 1 (Re«1). The Reynolds number (Re) relates the inertial and viscous forces in a fluid that is moving. Depending on the value of the Reynolds number, different regimes are possible. At high Reynolds numbers, turbulent flow occurs, which signifies the presence of comparatively large inertial forces. At low Reynolds numbers, laminar flow occurs with

comparatively larger viscous forces. Generally, the Reynolds number is defined as eq. (4) [35] [36].

$$Re = \frac{uL}{v} = \frac{\rho u L}{\mu} \tag{4}$$

More specifically, flow within a pipe or microchannel can be calculated from:

$$Re = \frac{uD_H}{v} = \frac{\rho u D_H}{\mu} = \frac{\rho Q D_H}{\mu A} = \frac{W D_H}{\mu A} \tag{5}$$

With the respective variables explained in table I. The hydraulic diameter (D_H) is based on a circular tube. In this study, a rectangular microchannel is assumed. Hence, the hydraulic diameter is redefined as:

$$D_H = \frac{4A}{P} = \frac{2WH}{W+H} \tag{6}$$

Where P is the wetted perimeter, in this case it is equal to 2(W+H).

TABLE I: Symbol list Reynolds number

Symbol	Description	Unit	Value
D_H	Hydraulic diameter	m	4.62×10^{-4}
Q	Volumetric flowrate	m^3/s	1.67×10^{-10}
A	Cross-sectional area	m^2	3×10^{-7}
u	Mean velocity in fluid	m/s	5.56×10^{-4}
μ	Dynamic viscosity	$Pa \cdot s$	1.002×10^{-3}
ν	Kinematic viscosity	m^2/s	1.004×10^{-6}
ρ	Density of fluid	kg/m^3	998
W	Mass flowrate of fluid	kg/s	1.66×10^{-7}

An approximate value of Re = 0.255 is found using the values provided in table I and eq. (5). The value is less than 1 and allows for the assumption of a low Reynolds number behaviour in the microfluidic channel, which means laminar flow. The inertial term can be neglected, which yields the Stokes equations:

$$\rho(\vec{u} \cdot \nabla)\vec{u} = \nabla \cdot [-p\mathbb{I} + \vec{K}] + \vec{F} \tag{7}$$

$$\rho(\vec{u} \cdot \nabla)\vec{u} = 0 \tag{8}$$

$$0 = \nabla \cdot [-p\mathbb{I} + \vec{K}] + \vec{F} \tag{9}$$

Here, $\vec{K}$ equals $\mu(\nabla\vec{u}+(\nabla\vec{u})^T)$ and $\mathbb{I}$ is the identity matrix. Under the assumption of an incompressible fluid, as described in eq. (10), eq. (9) simplifies to eq. (11).

$$\nabla \cdot \vec{u} = 0 \tag{10}$$

$$0 = \mu\nabla^2\vec{u} - \nabla\rho + \vec{F} \tag{11}$$

The simulation is built with a 2D model. To accurately represent the microfluidic channel, a drag term is introduced through the shallow channel approximation checkbox. This introduces a new term in the Stokes equation which models the resistance that the fluid experiences from parallel boundaries. The velocity field ($\vec{u}$) and the depth of the microchannel (d_z) are the variables that affect the flow. It does not account for possible changes in the velocity field due to the depth of the microchannel [33] [34]. The updated Stokes equation is eq. (12) with the variable d_z set to 300[μm].

$$0 = \mu\nabla^2\vec{u} - \nabla\rho - 12\frac{\mu\vec{u}}{d_z^2} + \vec{F} \tag{12}$$

The material constants and initial conditions for the creeping flow module are provided in table II.

TABLE II: Fluid parameters and initial conditions.

Parameter	Description	Unit	Value
ρ	Density	kg/m^3	998
μ	Dynamic viscosity	Pa·s	1.002×10^{-3}
Temperature in water	Initial condition	$°C$	20
Pressure in water	Initial condition	Pa	0

Boundaries conditions are necessary to enable functional and realistic simulations in COMSOL. In fig. 4 the boundary conditions and their locations are displayed. The details of these boundary conditions are shown in table III. For the creeping flow module, we assume a single fully developed flow. That means that the first and second boundary conditions are coupled.

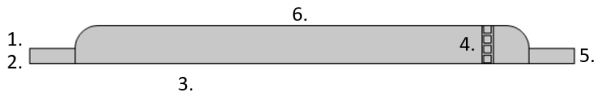

Fig. 4: 2D model locations boundary conditions

TABLE III: Boundary conditions creeping flow

B.C.	Location	Details	Equation
Inlet	1 & 2	Fully developed flow, flowrate: $10 \times 10^{-6}[L/min]$	$\vec{u} \cdot \vec{t} = 0$ $P_{\text{inl}} : V_0 = -\int_{\partial\Omega_{\text{inl}}} d_z \vec{u} \cdot \vec{n}\, dS$
Symmetry	3	X-axis	$\vec{u} \cdot \vec{n} = 0$
Wall	4 & 6	No slip	$\vec{u} = 0$
Outlet	5	Pressure, suppress backflow checkbox	$[-p\mathbb{I} + \vec{K}]\vec{n} = -\hat{p}_0\vec{n}$ $\hat{p}_0 \leq p_0$, p_0 = 0

In the creeping flow module, the two inlets are combined to generate a single fully developed flow with a flowrate (V_0) of 10×10^{-6} [L/min]. The boundary of symmetry is imposed on the x-axis of the 2D model, and the outlet has a pressure boundary condition of $p_0 = 0$. The backflow of the fluid is suppressed. The walls, including the particle sieves (4), have a no-slip boundary condition that sets the velocity field to zero near the walls.

2) Transport of diluted species: The transport of diluted species module introduces the Nernst Planck equations from eq. (13) into the 2D model [37].

$$\frac{\partial c_i}{\partial t} + \nabla \cdot \vec{N}_i = R_{i,tot} \tag{13}$$

More specifically, N_i consists of three sources; diffusion, convection, and migration [37].

$$N_i = -D_i \nabla c_i - z_i u_{m,i} F_{c_i} \nabla \phi_l + c_i \vec{u} = \vec{J_i} + c_i \vec{u} \quad (14)$$

$$Diffusion = -D_i \nabla c_i \quad (15)$$

$$Convection = c_i \vec{u} \quad (16)$$

$$Migration = -z_i u_{m,i} F_{c_i} \nabla \phi_l \quad (17)$$

Migration is not relevant for the scope of this study and is set to zero. This leaves the diffusion and convection components of the Nernst Planck equation in eq. (18).

$$\frac{\partial c_i}{dt} + \nabla \cdot [-D_i \nabla c_i + c_i \vec{u}] \quad (18)$$

In fig. 4 the locations of the boundary conditions for the transport of diluted species are shown. The details of each boundary condition can be found in table IV. The concentration is initially set to zero throughout the domain in the initial values subtab. An outflow boundary condition is applied to prevent horizontal diffusion across the boundary surface, while a no-flux condition ensures that no mass transfer occurs through the solid structures in the 2D simulation. Finally, a boundary condition for the symmetry is used along the x-axis to eliminate diffusion across it. The inflow is subdivided into two sections. The two inlets are separated by a small square (1 $[\mu m]$ by 1 $[\mu m]$) in the simulation to prevent unwanted boundary effects at the start of the two inlets. One inlet carries only water whilst the other inlet has a concentration mixed into the water. The diffusion coefficient D_i is set to 7×10^{-10} $[m^2/s]$. This is the approximate diffusion coefficient for materials such as rhodamine B (fluorescend dye) [38] and methylene blue (tracer dye) [39] between 23 ° and 25 ° Celcius. D_i varies with temperature according to the Stokes–Einstein–Sutherland equation seen in eq. (19) [40]. Here, K_B is the Boltzmann constant, T is the temperature, η is the dynamic viscosity, and r is the Stokes radius for a spherical particle.

$$D_i = \frac{K_B T}{6 \pi \eta r} \quad (19)$$

The temperature dependence of D_i is outside the scope of this study. However, it is important to note that D_i could dynamically change during physical experiments through pressure differences, cavitation of microbubbles, or microjetting generated by acoustic actuation. These phenomena are able to locally change temperatures, and hence change the local diffusion constant. The significance of these temperature changes depends on the duration and intensity of the acoustic actuation.

The Nernst Planck equations are the bedrock of the transport of diluted species module and are used in this study to simulate the effects of changing velocity fields due to acoustic actuation. These pressure fields and their acoustic behaviour are the focus of the following section.

TABLE IV: Boundary conditions transport of diluted species

B.C.	Location	Details	Equation
Inflow	1	$c_{0,c} = 1[mol/m^3]$	$c_i = c_{0,i}$
Inflow	2	$c_{0,c} = 0[mol/m^3]$	$c_i = c_{0,i}$
Symmetry	3	X-axis symmetry	$-\vec{n} \cdot \vec{J_i} = 0$
No flux	4 & 6	No flux through boundary	$-\vec{n} \cdot \vec{J_i} = 0$
Outflow	5	No diffusion in y-direction	$\vec{n} \cdot D_i \nabla c_i = 0$

3) Pressure acoustics, frequency domain: The pressure acoustics, frequency domain module is used to simulate the pressure fields that arise from applying an acoustic wave to the microfluidic channel. The general wave equation in a lossless medium is given in eq. (20) [41].

$$\frac{1}{\rho c^2} \frac{\partial^2 p}{\partial t^2} + \nabla \cdot (-\frac{1}{\rho}(\nabla p - \vec{q}_d)) = Q_m \quad (20)$$

There are two possible sources, Q_m as a monopole source and $\vec{q}_d$ as a dipole source. An inhomogeneous Helmholtz equation can be obtained by assuming a time-varying pressure with a time-harmonic wave like eq. (21). The angular frequency, ω, is equal to $2\pi f$. The same harmonic time dependence should hold for both sources (Q_m and $\vec{q}_d$) [41].

$$p(\vec{x}, t) = p(\vec{x}) e^{i\omega t} \quad (21)$$

$$\nabla \cdot (-\frac{1}{\rho_c}(\nabla p - \vec{q}_d)) - \frac{\omega^2 p}{\rho_c c_c^2} = Q_m \quad (22)$$

Depending on the choice of the 2D plane and the direction of the propagating wave, a more complete equation should be used. This equation is depicted in eq. (23). This is the equation COMSOL Multiphysics uses for its pressure acoustics, frequency domain module. It allows for the possibility of an out-of-plane wave (z-direction) to contribute to the 2D simulation.

$$\nabla \cdot (-\frac{1}{\rho_c}(\nabla p - \vec{q}_d)) - \frac{k_{eq}^2 p_t}{\rho_c} = Q_m \quad (23)$$

Where p_t is the total pressure defined as $p_t = p_b + p_s$. Here, p_b is the background pressure field and p_s is the scattered pressure field. The subscripted c in density ρ_c and speed of sound c_c in eq. (23) indicates the possibility of including complex-valued media (e.g. porous media). Furthermore, k_{eq} is the wave number with $k_{eq}^2 = (\frac{\omega}{c_c})^2 - k_z^2$. The 2D model is solved in the xy plane and the acoustic wave propagates in the y direction. Hence, we can set k_z to zero in eq. (23).

The pressure acoustics, frequency domain module covers a large part of the reactor chamber. It does not include the inlet, outlet or the particles sieves. The initial pressure is set to zero. Two different thermoviscous boundary layer impedances (T.B.L.I-1 and 2 in table V) are added as boundary conditions. The first thermoviscous boundary condition adds a no-slip mechanical condition to the model at the transitions of the

TABLE V: Boundary conditions pressure acoustics, frequency domain module,

B.C.	Location	Details	Equation
Symmetry	3	X-axis symmetry	$-\vec{n} \cdot (-\frac{1}{\rho_c}(\nabla p_t - \vec{q}_d)) = 0$
T.B.L.I - 1	6	Mechanical condition velocity	$Act_{v0} = 2\pi f_0 Act_{d0}$
T.B.L.I - 2	-	No-slip on walls	Mechanical condition: no-slip

inlet and outlet to the microreactor. The second thermoviscous boundary layer actuates a part of the wall of the microreactor to mimic the vibration of a piezoceramic resonator that would be glued to the microfluidic chip. A sinusoidal wave is applied to the boundary following eq. (24), where Act_{d0} is the amount of displacement in [nm] and f_0 is one of the resonance frequencies calculated with eq. (1).

$$Act_{v0} = 2\pi f_0 Act_{d0} \tag{24}$$

4) Thermoviscous acoustics, frequency domain: The thermoviscous acoustics, frequency domain module is used when relatively sharp boundary effects are possible in the simulation [42]. In this simulation, the particle sieves have relatively sharp boundaries compared to the rest of the microfluidic channel. Hence, an extra domain was added around the particle sieves to accommodate the module. The thermoviscous acoustics, frequency domain module is computationally significantly more demanding than the pressure acoustics, frequency domain module [42]. It is wise to use thermoviscous acoustics, frequency domain module only where needed to save both computational power and time. Only two boundary conditions are imposed on the small domain around the particle sieves in the microreactor. A symmetry condition is imposed on the symmetry axis in the domain and a no-slip mechanical condition is imposed on the particle sieve walls. The boundary conditions are given in table VI.

TABLE VI: Boundary conditions thermoviscous acoustics, frequency domain module

B.C.	Location	Details	Equation
Symmetry	3	X-axis symmetry	$\vec{n} \cdot \vec{u}_t = 0$ and $-\vec{n} \cdot (-k\nabla T_t) = 0$
Wall	4	No slip condition	Mechanical condition: no-slip

5) Multiphysics coupling: Several multi-physics interfaces are used to ensure that the physics interfaces are coupling appropriately. The transport of diluted species needs to be connected to the fluid flow in order to experience both convective and diffusive mass transport. This is done through the reacting flow, diluted species interface which couples the fluid flow and the species transport. The interface synchronises the velocity field of the creeping flow module with the velocity field of the transport of diluted species module [43]. The synchronisation of the velocity fields couples the diffusion and convection of the mass transport to the flow of the fluid in the microfluidic channel. Another multiphysics coupling interface is the acoustic streaming domain coupling. This interface couples the pressure acoustics, frequency domain module to the creeping flow module. The domain coupling interface ensures that effects in the domain area such as bulk streaming effects are appropriately linked [44]. It is used in conjuction with the acoustic streaming-boundary coupling interface. The boundary coupling interface ensures an appropriate representation of boundary-related streaming effects [45]. For the pressure acoustics, frequency domain module, the liquid should be set to thermally conducting and viscous. Moreover, if sharp boundaries occur in the simulation, the thermoviscous acoustics, frequency domain module should be used instead of the pressure acoustics, frequency domain module [45]. The thermoviscous acoustics, frequency domain has been used in the domain around the particle sieves, as relatively sharp boundaries are observed there. To couple the actuation from the pressure acoustics, frequency domain to the thermoviscous acoustics, frequency domain the acoustic-thermoviscous acoustic boundary interface is used in the multiphysics module. The thermoviscous acoustics, frequency domain interface is computationally more demanding than the pressure acoustics and is therefore only used at the sharp boundaries of the domain. The coupling equations are provided in eqs. (25) to (27). The variables used are described in table VII [46]. The first coupling equation essentially describes the continuity of the acoustic pressure from the pressure acoustics, frequency domain in the velocity field of the thermoviscous acoustics, frequency domain [46]. In addition, it describes a balance in momentum with eq. (26) and an adiabatic condition in eq. (27) to ensure that there is no heat flux across the boundary [46].

$$-\vec{n} \cdot (-\frac{1}{\rho_c}(\nabla p_t^{pa} - \vec{q}_d)) = -\vec{n} \cdot i\omega\vec{u}_t \text{ (Frequency domain)} \tag{25}$$

$$[p_t\mathbb{I} + \mu(\nabla\vec{u}_t + (\nabla\vec{u}_t)^T) - (\frac{2\mu}{3} - \mu_B)(\nabla \cdot \vec{u}_t)\mathbb{I}]\vec{n} = -p_t^{pa}\vec{n} \tag{26}$$

$$\vec{n} \cdot (-k\nabla T_t) = 0 \tag{27}$$

6) Simulation approach: To progressively build up the complexity of the simulation, the study was structured in three stages. This stepwise approach allows for a clearer understanding of how each physical interaction contributes to the overall system behaviour. In the first stage, the fluid flow and mass transport modules were coupled to examine their interaction in the absence of acoustic effects. In the second stage, a separate model was developed to couple fluid flow with acoustics, enabling the investigation of how ultrasonic actuation influences fluid dynamics. Finally, the three physics domains; fluid flow, acoustics, and mass transport, were integrated into a single comprehensive model to evaluate the

TABLE VII: Symbols in eqs. (25) to (27)

Symbol	Description	Unit
$\mathbf{n}$	Outward unit normal vector to boundary	–
ρ_c	Reference (ambient) density of the fluid	$\frac{kg}{m^3}$
p_t^{pa}	Acoustic pressure (pressure-acoustics interface)	Pa
p_t	Thermoviscous acoustic pressure variable	Pa
$\mathbf{q}_d$	Dipole (momentum) source term (same dimension as ∇p)	$\frac{Pa}{m}$
i	Imaginary unit	–
ω	Angular frequency	$\frac{rad}{s}$
$\mathbf{u}_t$	Acoustic particle velocity vector	$\frac{m}{s}$
$\mathbf{I}$	Identity tensor	–
μ	Dynamic (shear) viscosity	Pa s
μ_B	Bulk viscosity	Pa s
k	Thermal conductivity	$\frac{W}{mK}$
T_t	Acoustic temperature fluctuation	K
$\nabla(\cdot)$, $\nabla\cdot(\cdot)$	Gradient / divergence operators	–
$\partial/\partial t$	Time derivative	$\frac{1}{s}$

combined effects of ultrasonic actuation on mass transport in the microfluidic channel.

V. Results

A. Creeping flow and transport of diluted species

The first simulation built is the combination of the creeping flow and the transport of diluted species simulation. This simulation shows the at rest conditions of the system. The inlet has a flow rate of $10 \times 10^{-6}[\frac{L}{min}]$. The flow rate dominates the flow of the fluid as seen in fig. 5. The velocity profile in the y-direction is shown in fig. 6.

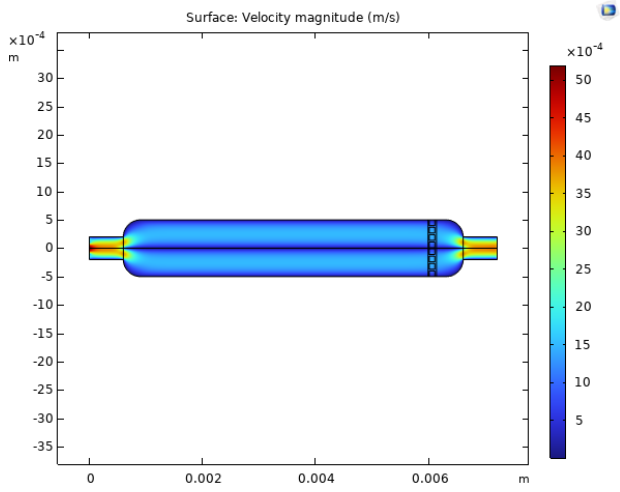

Fig. 5: Velocity magnitude without acoustic actuation

The diffusion component dominates in the concentration profile of fig. 7. This is due to the lack of convection in the y-direction. Following eq. (18), the convection component of the Nernst Planck equations is small compared to the diffusion component.

The Péclet number describes the ratio between the convection and diffusion components of the Nernst Planck equations and is defined in eq. (28).

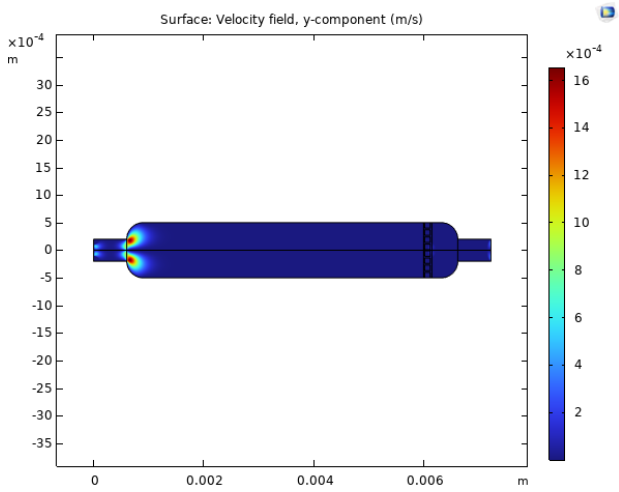

Fig. 6: Velocity in the y-direction without acoustic actuation

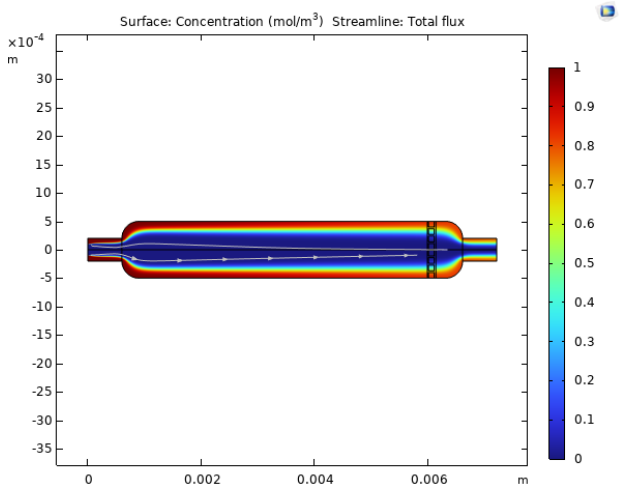

Fig. 7: Concentration profile without acoustic actuation

$$Pe_L = \frac{Lu}{D} = \frac{\frac{u}{L}}{\frac{D}{L^2}} = \frac{\frac{L^2}{D}}{\frac{L}{u}} \tag{28}$$

Where L is the characteristic length of the channel, u is the velocity component, and D is the diffusion constant. Essentially, the Péclet number in its last form describes the ratio of diffusion and convection in time. For a Péclet number $\gg 1$, the diffusion time is significantly longer than the convection time. Hence, convection dominates the concentration profile. Similarly for a Péclet number $\ll 1$, the convection time is significantly longer than the diffusion time, and thus diffusion dominates the concentration profile. Calculating the Péclet number from eq. (28) using the approximate velocity profile in the y direction of fig. 6 (5.1453×10^{-10} [m/s]), the characteristic length equal to 0.5 [mm] and the diffusion constant D being 7×10^{-10} yield a value of $\approx 3.68\times10^{-4}$. The inspection of fig. 7 and the calculation of the Péclet number for the simulation without acoustic actuation reveal that the

mass transport is dominated by the diffusion component of eq. (18).

B. Creeping flow and pressure acoustics, frequency domain

The second simulation model built is the creeping flow in conjunction with the pressure acoustics in the frequency domain modules. This simulation tests and visualises how acoustic waves are introduced in the microfluidic channel and how they take shape. In fig. 11 an acoustic wave is introduced by applying a sinusoidal actuation of 20 [nm] at 1.48 [MHz] to the upper wall segment of the microfluidic channel.

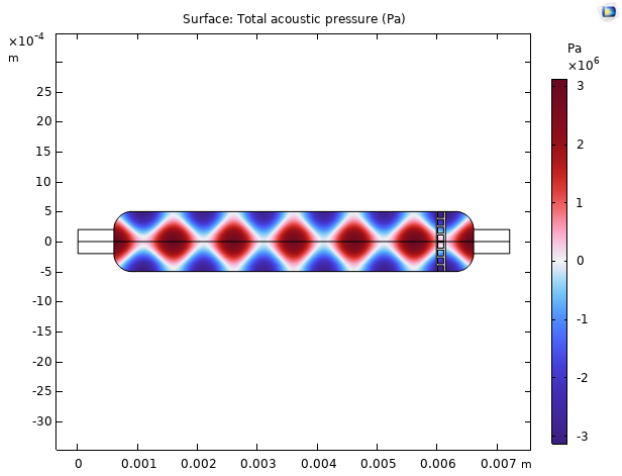

Fig. 8: Pressure acoustics at 20[nm] actuation and 1.48[MHz]

The acoustic pressure wave is coupled to the creeping flow module through the acoustic streaming domain coupling options in the Multiphysics tab in COMSOL Multiphysics. This generates the velocity magnitude profile from fig. 9 and the velocity profile in the y direction from fig. 10.

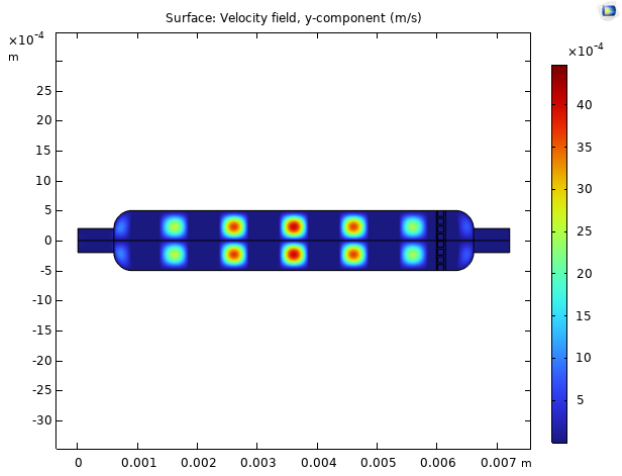

Fig. 9: Velocity component in the y-direction at 20[nm] actuation and 1.48[MHz]

Compared to fig. 5, the velocity magnitude profile has changed significantly and shows clear signs of differences in

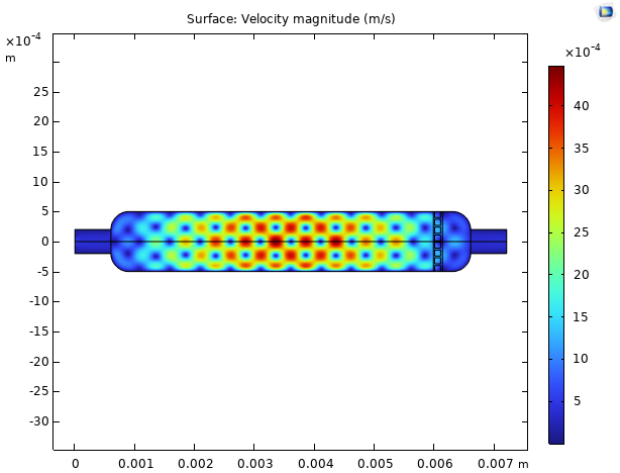

Fig. 10: Velocity magnitude at 20[nm] actuation and 1.48[MHz]

acoustic pressure in the microfluidic channel. This becomes even more clear when comparing fig. 6 to fig. 9. The pressure zones of fig. 8 overlap with the velocity increases in fig. 9 and are the reason for sudden velocity increases in the y component in the microfluidic channel.

C. Creeping flow, transport of diluted species and pressure acoustics, frequency domain

The third and final simulation model combines the three physics domains in one simulation model. The thermoviscous acoustics, frequency domain is used to calculate the behaviour of the acoustical waves around the particle sieves domain. The rest of the reactor channel is coupled to the pressure acoustics module in the frequency domain. The pressure acoustics are coupled to the creeping flow through the acoustic streaming domain coupling option. The creeping flow and transport of diluted species are coupled in a similar fashion through the Reacting Flow, Diluted Species Multiphysics tab. The sinusoidal actuation of 20 [nm] at 1.48 [MHz] to the top wall segment of the microfluidic channel generates the concentration profile seen in fig. 11. The diffusion constant D is $7 \times 10^{-10} [m^2/s]$.

The Péclet number can be calculated with values from fig. 9, the diffusion constant D, and the characteristic length of the channel following eq. (28). Calculating the Péclet number with the new velocity value ($\approx 1.298 \times 10^{-3}$ [m/s]) of fig. 9 yields a value of $\approx$ 1854.36. Both fig. 11 and the Péclet number indicate that mass transport is now heavily dominated by the convection component in eq. (18).

D. Differences in frequencies, actuation and diffusion constants

1) Frequency parameter: Following eq. (1), N can be any integer and yields a standing wave with singular or multiple nodes/antinodes. The frequency of 1.48 [MHz] comes from the integer N = 2. N = 1 yields a frequency of 0.74 [MHz] and N = 3 yields a frequency of 2.2215 [MHz] and so forth.

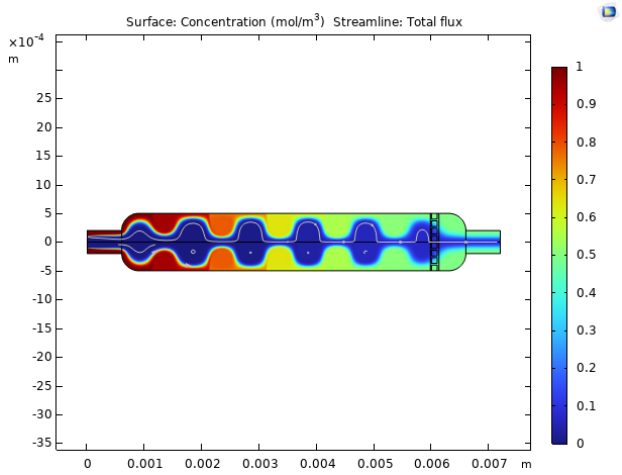

Fig. 11: Concentration profile at 20 [nm] actuation and 1.48 [MHz] with a diffusion constant of $7 \times 10^{-10}[m^2/s]$

The pressure plots for N = 1 to N = 8 are plotted in fig. 12 and fig. 13 at 20 [nm] actuation. The results are also provided in a larger format in section VIII-D.

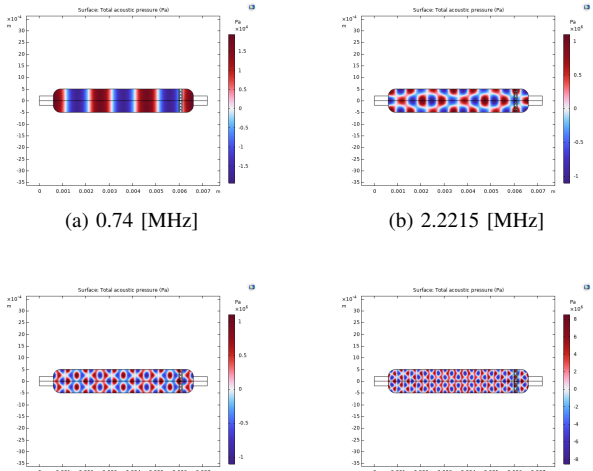

(a) 0.74 [MHz] (b) 2.2215 [MHz]

(c) 3.7025 [MHz] (d) 5.1835 [MHz]

Fig. 12: Acoustic pressure plots for N = 1, 3, 5, 7

In fig. 12 there are pressure nodes per wave that correspond to N = 1, 3, 5 and 7. Similarly, for fig. 13, there are pressure nodes per wave that correspond to N = 2, 4, 6 and 8. The velocities in the y direction for the respective frequencies are shown in fig. 14 and fig. 15.

Each velocity plot follows its respective acoustic pressure plot and generates different pressure gradients in the microfluidic channel. For completeness, the magnitude plots at 20nm actuation for N = 1 to N = 8 are included in section VIII-D. These different pressure gradients (and thus different velocity profiles) show different concentration profiles. These are shown in fig. 16 and fig. 17.

Comparison and examination of the concentration plots for uneven integers (fig. 16) versus even integers (fig. 17) show

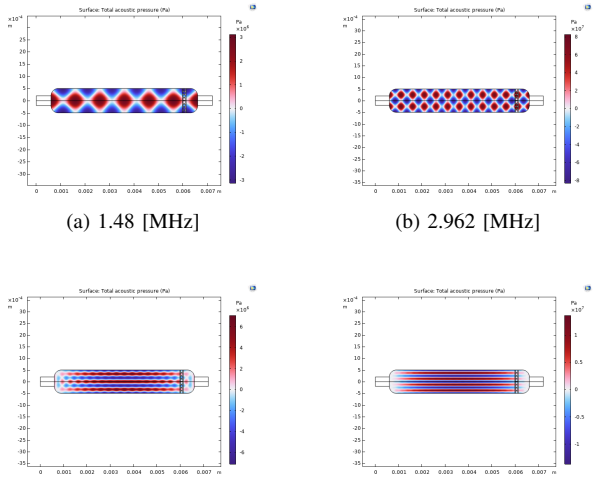

(a) 1.48 [MHz] (b) 2.962 [MHz]

(c) 4.443 [MHz] (d) 5.924 [MHz]

Fig. 13: Acoustic pressure plots for N = 2, 4, 6, 8

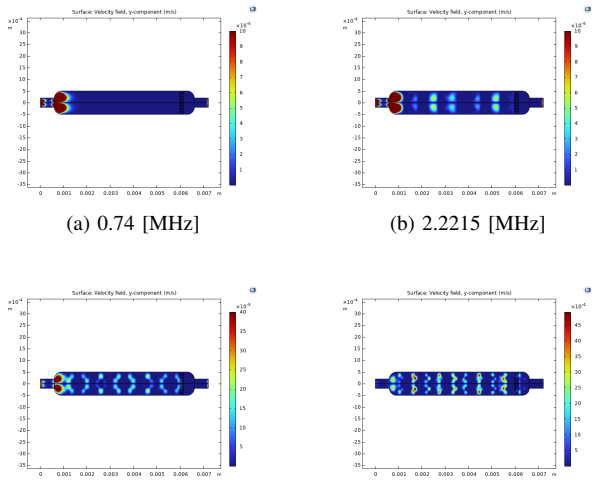

(a) 0.74 [MHz] (b) 2.2215 [MHz]

(c) 3.7025 [MHz] (d) 5.1835 [MHz]

Fig. 14: Velocity in the y-direction plots for N = 1, 3, 5, 7

that the mixing index improves significantly when using even integer numbers. The frequency is determined by the integer choice. This can be explained by examining fig. 12. Each uneven integer plot shows nodes at the boundaries of the microfluidic channel, while even integer plots show nodes at the centre of the microfluidic channel. The placement of these nodes and antinodes significantly impacts the mixing efficiency in the microfluidic channel. As N becomes larger for uneven plots, more nodes are distributed across the microfluidic channel, and the concentration profile improves. This improvement can be seen in fig. 14d versus the rest of the subplots (figs. 14a to 14c).

2) Actuation parameter: Another important factor that affects the performance of acoustic pressure waves is the actuation parameter. The initial results were tested with an actuation parameter of 20 [nm]. The behaviour of the actuation parameter at 10 [nm] is investigated here. The most interesting

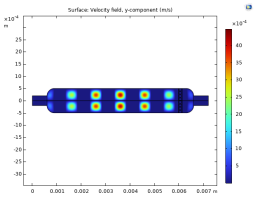

(a) 1.48 [MHz]

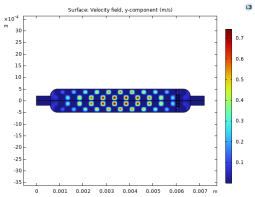

(b) 2.962 [MHz]

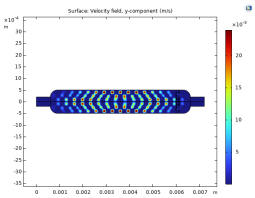

(c) 4.443 [MHz]

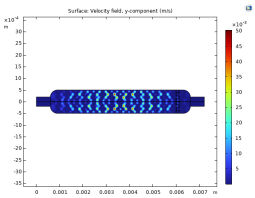

(d) 5.924 [MHz]

Fig. 15: Velocity in the y-direction plots for N = 2, 4, 6, 8

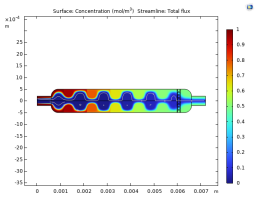

(a) 1.48 [MHz]

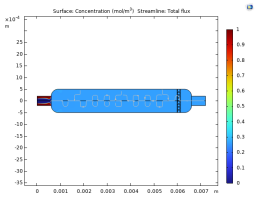

(b) 2.962 [MHz]

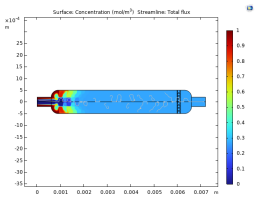

(c) 4.443 [MHz]

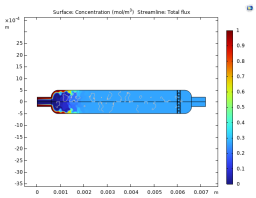

(d) 5.924 [MHz]

Fig. 17: Concentration gradient plots for N = 2, 4, 6, 8

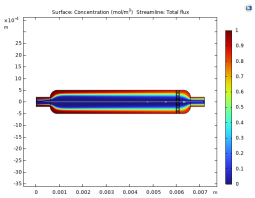

(a) 0.74 [MHz]

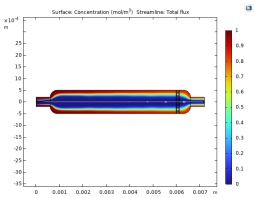

(b) 2.2215 [MHz]

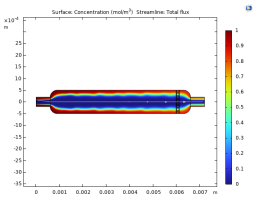

(c) 3.7025 [MHz]

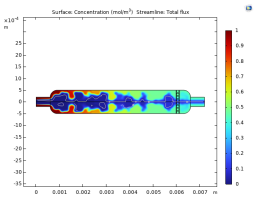

(d) 5.1835 [MHz]

Fig. 16: Concentration gradient plots for N = 1, 3, 5, 7

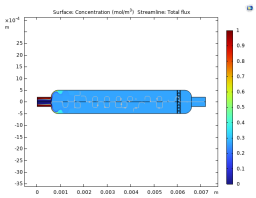

(a) 2.962 [MHz] (N = 4)

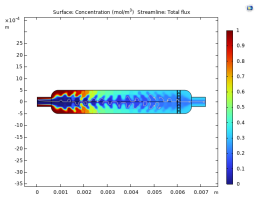

(b) 4.443 [MHz] (N = 6)

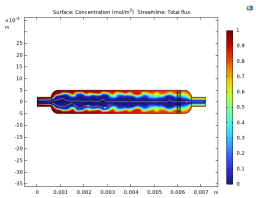

(c) 5.1835 [MHz] (N = 7)

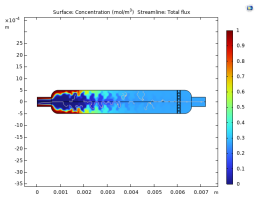

(d) 5.924 [MHz] (N = 8)

Fig. 18: Concentration gradient plots for N = 4, 6, 7 and 8

results are shown, and the complete results are added to section VIII-D. The best concentration gradient plots are provided in fig. 18.

From the subplots in fig. 18, fig. 18a stands out the most, as it shows the fastest mixing in the concentration profile. The acoustic pressure is a key factor here. The acoustic pressure experienced by fig. 18a is at its maximum 40 [MPa], whereas the other subplots experience maxima of 3.5 [MPa] (fig. 18b), 4 [MPa] (fig. 18c) and 6.5 [MPa] (fig. 18d). The respective acoustic pressure plots can be found in section VIII-D. Moreover, results for 2.962 [MHz] at 2.5 [nm] and 5 [nm] actuation are included in section VIII-D as well.

3) Convection vs diffusion: The Péclet number is influenced by the velocity component in the y direction. Reducing the actuation from 20 [nm] to 10 [nm] has a significant impact on the dominance of convection in mass transport. Similarly, increasing the actuation pattern from 20 [nm] to 30 [nm] increases the dominance of convection in mass transport. Some examples of calculations are shown in table VIII . These values are calculated at 1.48 [MHz] using 1 [mm] as the characteristic length L and D = $7 \times 10^{-10} [m^2/s]$ with eq. (28). More values based on 2.2215 [MHz] are provided in table IX.

Actuation [nm]	X [m]	Y [m]	Velocity y-component [m/s]	Péclet number
5	0.0036047	2.46×10^{-4}	2.51×10^{-4}	358.6
10	0.0035956	2.06×10^{-4}	9.94×10^{-4}	1420
20	0.0035997	2.22×10^{-4}	4.03×10^{-3}	5758
30	0.0035986	2.12×10^{-4}	9.01×10^{-3}	1.29×10^{4}

TABLE VIII: Velocity and Péclet number for different piezo actuation amplitudes at 1.48 [MHz]

Actuation [nm]	X [m]	Y [m]	Velocity y-componen [m/s]	Péclet number
5	0.0024963	1.85×10^{-4}	3.81×10^{-6}	5.44
10	0.0024828	1.84×10^{-4}	1.51×10^{-5}	21.55
20	0.0024977	1.88×10^{-4}	6.08×10^{-5}	86.88
30	0.0024923	1.78×10^{-4}	1.37×10^{-4}	195.4

TABLE IX: Velocity and Péclet number for different piezo actuation amplitudes at 2.2215 [MHz]

4) Diffusion constant: In the 2D simulation model, some issues were encountered when simulating the model with a lower value of D. For the value of $4.5 \times 10^{-10}[m^2/s]$, the model had trouble converging the solution and remained stuck in the 10^{-5} region (10^{-6} would allow it to converge). The main factors believed to influence the convergence issue are the diffusion pattern and the granularity of the mesh. A lower diffusion constant means slower mass transport. A refined mesh that is adjusted according to the diffusion pattern could aid in solving for lower diffusion constants by paying more attention to key areas in the microreactor. Creating this mesh was outside of the scope of this study.

E. Limitations of the simulation model

1) 2D simulations: One of the limitations of the simulation model is that the model is designed in 2D. This design choice significantly reduces the complexity of the simulation model at the cost of accuracy and representability. The choice for 2D allows for a large reduction in simulation time when compared with 3D models. The increase in time required by a 3D model accumulates over weeks of simulations. Thus, to prevent issues with time constraints in the study, a 2D model was made. One of the constraints with a 2D model is that mass-transport of the diluted species and the Stokes flow are restricted to 2D space whereas a real reactor would include a third dimension in which mass-transport or fluid flow could occur. To combat this in the fluid flow domain, the shallow-channel approximation was used. This approximation adds a drag term to the governing Stokes equation that takes into account the out-of-plane boundaries (top and bottom of the channel). For mass transport, this phenomenon becomes increasingly more important as the pressure acoustics are added to the microfluidic reactor channel. The dimension of the microfluidic channel determine the resonance frequencies in different domains. In eq. (1), the wavelength is used to determine the resonance frequency. Replacing the wavelength (λ) with 2h, with h being a dimension of the microfluidic channel, results in various resonance frequencies for each dimension of the microfluidic channel. For N = 1, with dimensions 1x6x0.3 [mm] the resonance frequencies in ambient water are 0.7405 [MHz], 0.1234 [MHz] and 2.4683 [MHz]. The 1 [mm] value used in the current 2D setup includes higher frequencies for a higher value of N and among these higher frequencies are values relatively close to the 2.4683 [MHz] value for N = 1 with 0.3 [mm] (e.g. 2.2215 [MHz] (N=3) or 2.962 [MHz] (N=4)). This imposes a respresentability risk for the simulation model as two standing waves might form, one in the 2D plane and one in the out-of-plane dimension in real life.

2) Bonding of the piezoceramic resonator: The piezoceramic resonator is not modeled in the 2D simulation since that is outside the scope of this study. Nevertheless, it is an important consideration for the representability and accuracy of the 2D model. The bonding of the piezoceramic resonator to the microfluidic chip influences the power transfer from the piezoceramic resonator to the microfluidic chip. In this simulation, the bonding is assumed to be ideal which means the actuation parameter is directly correlated to the power transfer of the piezoceramic resonator. The change in height from the piezo follows from eq. (29) assuming no acting force on the piezoceramic resonator [47]:

$$\Delta h = d_{33} V \tag{29}$$

Here Δh is the height change due to actuation, d_{33} is the charge constant and V is the applied voltage in [V]. However, how well this energy is transferred to the microfluidic channel depends strongly on the bonding of the piezoceramic resonator to the microfluidic chip. The piezoceramic resonator will likely be glued to the microfluidic chip which could cause non-negligible attentuation of energy. Furthermore, the piezoceramic resonator itself has a coupling factor (k_{eff}) which determines how efficient the conversion from electrical to mechanical energy is [47]. The coupling factor is defined as:

$$k_{eff}^2 = \frac{\text{Converted energy}}{\text{Input energy}} \tag{30}$$

The coupling factor k_{eff} strongly depends on the proximity of the actuation frequency to one of the resonance frequencies of the piezoceramic resonator. In conclusion, the relationship between voltage and mechanical actuation strongly depends on the type of material used (d_{33}) [47]. The value of d_{33} varies between suppliers and should be characterised after the ordered piezoceramic resonators have arrived. The same holds for the k_{eff} value. After these parameters are tested, the damping factor of the bonding between the piezoceramic resonator and the microfluidic chip can be characterised. Alternatively, a higher voltage can be used to circumvent these non-ideal damping factors. To provide some context, several initial actuation voltages are calculated with a value of $460 \times 10^{-12}[\frac{C}{N}]$ for d_{33} [47] and assuming ideal power transfer and coupling in table X.

Actuation [nm]	5	10	20	30
Voltage [V]	10.87	21.74	43.48	65.22

TABLE X: Voltage required to obtain the indicated actuation amplitudes

3) Temperature dependence: In the 2D simulation model, temperature variations were not taken into account as it was outside the scope of the study. However, temperature changes are likely present in the microfluidic channel as a result of the introduction of pressure acoustics. These pressure acoustics generate pressure differences that are likely to introduce local temperature variations. Furthermore, strong acoustical actuation possibly enables cavitation effects and microjetting. The cavitation phenomena is explained in detail in section VIII-B. These local temperature variations can result in different results in real life. Two important variables are dependent on temperature; the diffusion constant D and the viscosity of the fluid. The diffusion constant D for molecules in a viscous fluid is called the Stokes-Einstein equation [48]. It is defined as:

$$D = \frac{kT}{6\pi\mu r} \tag{31}$$

The respective variables are explained in table XI. Temperature (T) is an important variable within the diffusion constant D as seen in eq. (31). Similarly, viscosity has several approximations that depend on temperature in various ways [49] [50]. All in all, the local variation in temperature and hence the local variation in diffusion constant D and the local variation in viscosity are not taken into account in the 2D simulation model.

Symbol	Description	Unit	Value
T	Temperature	Degrees Celsius	-
k	Boltzmann constant	$\frac{J}{K}$	1.380649×10^{-23} [51]
μ	Solvent viscosity	Pa·s	–
r	Radius of diffusing particle	m	–

TABLE XI: Overview of variables in eq. (31) [48]

VI. Conclusion

This thesis has examined the influence of acoustical actuation on the fluid flow and mass transport in a microfluidic reactor channel using COMSOL Multiphysics. Three domains; fluidics, mass transport, and acoustics, were successfully merged into a single simulation model. One of the notable results was the importance of frequency choice. The use of even integers in eq. (1) resulted in the placement of nodes in the middle of the channel, while uneven integers resulted in the placement of nodes at the boundaries of the microfluidic channel. This placement of the nodes had a significant impact on the concentration profile in the microfluidic channel. In general, even nodes had a significantly improved concentration profile. In addition, lower actuation was necessary to accommodate the improved concentration profile. The optimal frequency for both the concentration profile and the acoustic pressure found within the integers N = 1 to N = 8 was 2.962 [MHz] (N = 4). Even at lower actuations, such as 5 [nm], the concentration profile was better than most other integers (at 20 [nm]). In general, a clear dominance of convection was observed in most of the simulations.

In the current simulation, concentration is prescribed at the inlet; however, the overarching goal behind this study is to capture concentration changes driven by reactions at the mineral surface of olivine and to explore strategies to enhance those reaction rates. Accurately modeling these effects requires important modifications to the mass transport boundary conditions and adjustments to the fluid dynamics to reflect partial flow obstruction in a packed bed configuration. Due to time constraints, these complexities are beyond the scope of this study. In conclusion, the introduction of acoustic actuation to microfluidic channels greatly impacts the fluid flow and mass transport in the microfluidic channel if it is tuned to the dimensions of the microfluidic channel. Moreover, even integer variants of the resonance frequency are able to deliver more acoustic pressure to the microfluidic channel through the more optimal placement of nodes throughout the channel. The findings of this study lay the foundation for the future integration of surface reaction modeling and physical testing. They offer a promising direction for enhancing mineral-fluid interactions in acoustically actuated microfluidic systems.

A. Recommendations for future research

Important to note is that the model was simulated in 2D, which has its limitations. Future research can explore several topics. These include the addition of olivine particles to the simulation through the porous media options in COMSOL and building of a 3D simulation with the goal of investigating whether actuating the bottom of the channel brings (un)desirable side effects. Additionally, a refined mesh can be made to accommodate the convergence difficulties with the diffusion constant D. Furthermore, a plan of action has been provided in section VIII-E to kickstart physical experiments regarding both mixing experiments and olivine experiments after the piezoceramic resonators have been characterised.

References

[1] "Climate change 2023: Synthesis report. contribution of working groups i, ii and iii to the sixth assessment report of the intergovernmental panel on climate change," Intergovernmental Panel on Climate Change. (2023), [Online]. Available: https://www.ipcc.ch/report/sixth-assessment-report-cycle/ (visited on 10/18/2024).

[2] "Overview of greenhouse gases," United States Environmental Protection Agency. (2024), [Online]. Available: https://www.epa.gov/ghgemissions/overview-greenhouse-gases (visited on 12/09/2024).

[3] "Greenhouse gas emissions by country and sector (infographic)," European Parliament. (2024), [Online]. Available: https://www.europarl.europa.eu/topics/en/article/20180301STO98928/greenhouse-gas-emissions-by-country-and-sector-infographic (visited on 12/09/2024).

[4] "Carbon sequestration," Britannica. (2024), [Online]. Available: https://www.britannica.com/technology/carbon-sequestration (visited on 11/22/2024).

[5] "What is carbon sequestration?" United States Geological Survey. (), [Online]. Available: https://www.usgs.gov/faqs/what-carbon-sequestration (visited on 11/22/2024).

[6] "Permanent, fully verifiable co2 storage," Paebbl. (), [Online]. Available: https://paebbl.com/store-co2 (visited on 07/05/2025).

[7] M.-L. H. Kleinsmit, "Design, fabrication and validation of microreactors to study olivine carbonation in-operando with high-throughput," Master's thesis, University of Twente, Jul. 2023.

[8] "Cement and concrete: The environmental impact," Princeton Student Climate Initiative. (2020), [Online]. Available: https://psci.princeton.edu/tips/2020/11/3/cement-and-concrete-the-environmental-impact (visited on 11/22/2024).

[9] "Cement is a big problem for the environment. here's how to make it more sustainable," World Economic Forum. (), [Online]. Available: https://www.weforum.org/stories/2024/09/cement-production-sustainable-concrete-co2-emissions/ (visited on 11/22/2024).

[10] O. Sissmann, D. Daval, F. Guyot, *et al.*, "The deleterious effect of secondary phases on olivine carbonation yield: Insight from time-resolved aqueous-fluid sampling and fib-tem characterization," *Chemical Geology*, vol. 357, pp. 186–202, 2013.

[11] R. Santos, D. François, G. Mertens, J. Elsen, and T. van Gerven, "Ultrasound-intensified mineral carbonation," *Applied Thermal Engineering*, vol. 57, pp. 154–163, 2013.

[12] D. P. Thomas, J. Zhang, N.-T. Nguyen, and H. T. Ta, "Microfluidic gut-on-a-chip: Fundamentals and challenges," *Biosensors*, vol. 13, no. 1, p. 136, Jan. 2023. DOI: 10.3390/bios13010136. [Online]. Available: https://www.mdpi.com/2079-6374/13/1/136.

[13] S. Ó. Snæbjörnsdóttir, B. Sigfússon, C. Marieni, D. Goldberg, S. R. Gíslason, and E. H. Oelkers, "Mineral storage of co2," *Nature Reviews Earth and Environment*, vol. 1, no. 2, pp. 90–102, 2020.

[14] A. Sanna, M. Uibu, G. Caramanna, R. Kuusik, and M. Maroto-Valer, "A review of mineral carbonation technologies to sequester co2," *Chemical Society Reviews*, vol. 43, pp. 8049–8080, 2014. DOI: 10.1039/C4CS00035H.

[15] A. A. Olajire, "A review of mineral carbonation technology in sequestration of co2," *Journal of Petroleum Science and Engineering*, vol. 109, pp. 364–392, Sep. 2013. DOI: 10.1016/j.petrol.2013.03.013. [Online]. Available: https://www.sciencedirect.com/science/article/pii/S0920410513000673#s0020.

[16] B. Garcia, V. Beaumont, E. Perfetti, *et al.*, "Experiments and geochemical modelling of co2 sequestration by olivine: Potential, quantification," *Applied Geochemistry*, vol. 25, pp. 1383–1396, 9 Sep. 2010. DOI: 10.1016/j.apgeochem.2010.07.004. [Online]. Available: https://www.sciencedirect.com/science/article/pii/S0883292710001472.

[17] T. Zhu, L. Zheng, F. Li, J. Liu, and W. Zhuang, "Sustainable carbon sequestration via olivine based ocean alkalinity enhancement in the east and south china sea: Adhering to environmental norms for nickel and chromium," *Science of The Total Environment*, vol. 930, Jun. 2024. DOI: 10.1016/j.scitotenv.2024.172853. [Online]. Available: https://www.sciencedirect.com/science/article/pii/S0048969724030006.

[18] F. Montserrat, P. Renforth, J. Hartmann, M. Leermakers, P. Knops, and F. J. R. Meysman, "Olivine dissolution in seawater: Implications for co2 sequestration through enhanced weathering in coastal environments," *Environmental Science and Technology*, vol. 51, no. 7, pp. 3960–3972, Dec. 2024. DOI: 10.1021/acs.est.6b05942. [Online]. Available: https://pubs.acs.org/doi/10.1021/acs.est.6b05942.

[19] B. Wang, X. Gao, J. Song, *et al.*, "Feasibility of increasing marine carbon storage through olivine addition," *Journal of Environmental Chemical Engineering*, vol. 11, 6 Dec. 2023. DOI: 10.1016/j.jece.2023.111221. [Online]. Available: https://www.sciencedirect.com/science/article/pii/S2213343723019607.

[20] H. Beärat, M. J. McKelvy, A. V. G. Chizmeshya, *et al.*, "Carbon sequestration via aqueous olivine mineral carbonation: Role of passivating layer formation," *Environmental Science and Technology*, vol. 40, no. 15, pp. 4802–4808, 2006. DOI: 10.1021/es0523340.

[21] M. L. Iozzia, F. Goto, A. Podestà, *et al.*, "Olivine nanoparticles for fast atmospheric co2 capture at ambient conditions," *Particles and Particle Systems Characterization*, Jul. 2024. DOI: 10.1002/ppsc.202400063. [Online]. Available: https://onlinelibrary.wiley.com/doi/full/10.1002/ppsc.202400063.

[22] K. Yasui, *Acoustic Cavitation and Bubble Dynamics*. 2018. DOI: 10.1007/978-3-319-68237-2. [Online]. Available: https://www.springer.com/series/15634.

[23] T. Segers and M. Versluis, "Acoustic bubble sorting for ultrasound contrast agent enrichment," *Lab on a Chip*, vol. 14, pp. 1705–1714, 2014.

[24] R. Wagterveld, L. Boels, M. Mayer, and G. Witkamp, "Visualization of acoustic cavitation effects on suspended calcite crystals," *Ultrasonics Sonochemistry*, vol. 18, pp. 216–225, 2011.

[25] S. Medya and S. Yeo, "Enhancement of acoustic cavitation streaming: A study on surface finishing of additively manufactured components," *CIRP Journal of Manufacturing Science and Technology*, vol. 53, pp. 1–16, Oct. 2024. DOI: 10.1016/j.cirpj.2024.09.002. [Online]. Available: https://www.sciencedirect.com/science/article/pii/S1755581724000993.

[26] X. Zhu, R. S. Das, M. L. Bhavya, M. Garcia-Vaquero, and B. K. Tiwari, "Acoustic cavitation for agri-food applications: Mechanism of action, design of new systems, challenges and strategies for scale-up," *Ultrasonics Sonochemistry*, vol. 105, May 2024. DOI: 10.1016/j.ultsonch.2024.106850. [Online]. Available: https://www.sciencedirect.com/science/article/pii/S1350417724000981.

[27] C. C. Coussios and R. A. Roy, "Applications of acoustics and cavitation to noninvasive therapy and drug delivery," *Annual Review of Fluid Mechanics*, vol. 40, no. 1, pp. 395–420, 2008. DOI: 10.1146/annurev.fluid.40.111406.102116. [Online]. Available: https://ora.ox.ac.uk/objects/uuid:d1baf396-d51c-4a49-bd81-2a152819208d/download_file?file_format=pdf&safe_filename=ARFMFullPaperFinal2.pdf&type_of_work=Journal+article.

[28] N. S. M. Yusof, B. Babgi, Y. Alghamdi, M. Aksu, J. Madhavan, and M. Ashokkumar, "Physical and chemical effects of acoustic cavitation in selected ultrasonic cleaning applications," *Ultrasonics Sonochemistry*, vol. 29, pp. 568–576, Mar. 2016. DOI: 10.1016/j.ultsonch.2015.11.009. [Online]. Available: https://www.sciencedirect.com/science/article/pii/S1350417715001856.

[29] N. I. of Standards and Technology, *Isothermal properties for carbon dioxide*, NIST Chemistry WebBook. [Online]. Available: https://webbook.nist.gov/cgi/fluid.cgi?T=20&PLow=0.0&PHigh=80&PInc=1&Digits=5&ID=C124389&Action=Load&Type=IsoTherm&TUnit=C&PUnit=bar&DUnit=mol%2Fl&HUnit=kJ%2Fmol&WUnit=m%2Fs&VisUnit=uPa*s&STUnit=N%2Fm&RefState=DEF (visited on 11/22/2024).

[30] "Basic sound calculations," Piezo Technologies. (), [Online]. Available: https://piezotechnologies.com/basic-sound-calculations/ (visited on 11/27/2024).

[31] F. Ebrahimi, *Piezoelectric Materials and Devices - Practice and Applications*. 2013. DOI: 10.5772/45936. [Online]. Available: https://www.intechopen.com/books/3272.

[32] "Navier-stokes equations," COMSOL Multiphysics. (), [Online]. Available: https://www.comsol.com/multiphysics/navier-stokes-equations (visited on 07/04/2025).

[33] "The creeping flow interface," COMSOL Multiphysics. (), [Online]. Available: https://doc.comsol.com/6.0/doc/com.comsol.help.cfd/cfd_ug_fluidflow_single.06.007.html (visited on 07/04/2025).
[34] "The laminar flow interface," COMSOL Multiphysics. (), [Online]. Available: https://doc.comsol.com/6.0/doc/com.comsol.help.cfd/cfd_ug_fluidflow_single.06.008.html#5429372 (visited on 07/04/2025).
[35] "The reynolds number," COMSOL Multiphysics. (), [Online]. Available: https://doc.comsol.com/5.5/doc/com.comsol.help.comsol/comsol_ref_fluidflow.20.08.html (visited on 07/04/2025).
[36] P. J. LaNasa and E. L. Upp, *Fluid Flow Measurement - A Practical Guide to Accurate Flow Measurement*. Butterworth-Heinemann, 2014. DOI: 10.1016/C2011-0-07523-3. [Online]. Available: https://www.sciencedirect.com/book/9780124095243/fluid-flow-measurement.
[37] "The nernst–planck equations interface," COMSOL Multiphysics. (), [Online]. Available: https://doc.comsol.com/5.6/doc/com.comsol.help.chem/chem_ug_chemsptrans.08.126.html (visited on 07/04/2025).
[38] P. Kapusta, "Diffusion coefficients of common fluorescent dyes in water," PicoQuant GmbH, Application Note Rev. 1, 2010, Accessed: 2025-06-23. [Online]. Available: https://www.picoquant.com/images/uploads/page/files/7353/appnote_diffusioncoefficients.pdf.
[39] M. N., L. M., N. U., Ž.-P. P., and P. I., "Evaluation of diffusion coefficient determination using a microfluidic device.," *Chemical and biochemical engineering quarterly*, vol. 28, no. 2, pp. 215–223, 2014. DOI: 10.1021/es0523340.
[40] C. C. Miller, "The stokes-einstein law for diffusion in solution," *Proceedings of the Royal Society London A*, vol. 106, pp. 724–749, 2014. DOI: 10.1098/rspa.1924.0100.
[41] "The governing equations," COMSOL Multiphysics. (), [Online]. Available: https://doc.comsol.com/5.5/doc/com.comsol.help.aco/aco_ug_pressure.05.125.html#1060354 (visited on 07/04/2025).
[42] "The thermoviscous acoustics, frequency domain interface," COMSOL Multiphysics. (), [Online]. Available: https://doc.comsol.com/5.5/doc/com.comsol.help.aco/aco_ug_thermo.09.02.html (visited on 07/04/2025).
[43] "The reacting flow, diluted species coupling feature," COMSOL Multiphysics. (), [Online]. Available: https://doc.comsol.com/6.0/doc/com.comsol.help.cfd/cfd_ug_chemsptrans.11.083.html (visited on 07/04/2025).
[44] "Acoustic streaming domain coupling," COMSOL Multiphysics. (), [Online]. Available: https://doc.comsol.com/6.1/doc/com.comsol.help.aco/aco_ug_multiphysics_couplings.14.25.html (visited on 07/04/2025).
[45] "Acoustic streaming boundary coupling," COMSOL Multiphysics. (), [Online]. Available: https://doc.comsol.com/6.1/doc/com.comsol.help.aco/aco_ug_multiphysics_couplings.14.26.html#685038 (visited on 07/04/2025).
[46] "Acoustic-thermoviscous acoustic boundary," COMSOL Multiphysics. (), [Online]. Available: https://doc.comsol.com/5.5/doc/com.comsol.help.aco/aco_ug_multiphysics_couplings.13.06.html (visited on 07/04/2025).
[47] J. Waanders, *Acoustic Cavitation and Bubble Dynamics*. N. V. Philips' Gloeilampenfabrieken, 1991. [Online]. Available: https://www.ultrasonic-resonators.org/misc/references/articles/Waanders__'Piezoelectric_Ceramics__Properties_and_Applications'.pdf.
[48] "Diffusion coefficient," COMSOL Multiphysics. (2017), [Online]. Available: https://www.comsol.com/multiphysics/diffusion-coefficient (visited on 07/03/2025).
[49] "Formulas for viscosity," Cambridge-MIT Institute. (), [Online]. Available: http://www-mdp.eng.cam.ac.uk/web/library/enginfo/aerothermal_dvd_only/aero/fprops/propsoffluids/node5.html (visited on 07/03/2025).
[50] "Arrhenius equation," Britannica. (2025), [Online]. Available: https://www.britannica.com/science/Arrhenius-equation (visited on 07/03/2025).
[51] "Boltzmann constant," Britannica. (2025), [Online]. Available: https://www.britannica.com/science/Boltzmann-constant (visited on 07/03/2025).
[52] "Piezoceramic plates, wafers, bars and wedges," CTS Ferroperm Piezoceramics. (), [Online]. Available: https://www.ctscorp.com/Products/Piezoelectric/Bulk-Piezoceramics/Plates-wafers-bars-wedges (visited on 11/25/2024).

VII. AI STATEMENT

During the preparation of this work the author used Grammarly in order to filter out spelling and formulation mistakes. Furthermore, the author used ChatGPT (GPT-4) for feedback on pieces of text and for brainstorming purposes. After using these tools/services, the author reviewed and edited the content as needed and takes full responsibility for the content of the work.

VIII. APPENDIX

A. Planning

The planning of this thesis takes into account the workflow of table XII and the required writing and preparation for the final report and presentation.

TABLE XII: Workflow of the thesis

Task	Check
Practise with COMSOL library	✓
Sim 1. Fluid flow and mass transport	✓
Sim 2. Fluid flow and acoustics	✓
Sim 3. Fluid flow, mass transport and acoustics	✓
Write methodology	✓
Write results and discussion	✓
Write conclusion	✓
Adjust literature review	✓
Adjust abstract	✓
Process feedback on thesis	✓
Prepare thesis presentation	✓

B. Bubble resonance and collapse

It is important to understand how the cavitation process comes about and how it can be induced. The time-dependent radius of a bubble in a liquid can be described by the Rayleigh-Plesset equation. The Rayleigh-Plesset equation can be derived from the work required to expand a spherical bubble (and the liquid surrounding it) by dR and the kinetic energy that this process requires. By differentiating these terms we can find the Rayleigh-Plesset equation:

$$R\ddot{R} + \frac{3}{2}\dot{R}^2 = \frac{1}{\rho_0}[p_g + p_v - \frac{2\sigma}{R} - \frac{4\mu\dot{R}}{R} - \rho_0 - p_s(t)] \quad (32)$$

Violent bubble cavitation can be explained using the Rayleigh-Plesset equation if a spherical liquid around the spherical bubble is assumed. This is more commonly known

as the Rayleigh collapse. During the rarefraction phase of the ultrasound, bubbles expand and contract, and hence the ambient bubble radius shifts. When it reaches a critical point, the bubble wall collapses. According to Yasui, bubble pulsation is strongly non-linear when evaluated at higher acoustic amplitudes [22]. It is possible that at higher acoustic pressure amplitudes, the ambient range of bubble radii does not include the linear resonance frequency that was calculated through eq. (38). The lower bound of this range can be calculated using the Blake threshold radius (found in eq. (33)) and the upper bound of the range has the same magnitude as the linear resonance frequency calculated in eq. (38) [22].

$$p_{Blake} = p0 + \frac{8\sigma}{9}\sqrt{\frac{3\sigma}{2R_{0,Blake}^3[p_o + (2\sigma/R_{0,Blake}]}} \quad (33)$$

The eq. (33) describes the Blake pressure threshold (ultrasonic pressure amplitude) as a function of the Blake threshold radius (lower bound for the range of ambient radii for which a bubble actively pulses).

The Rayleigh collapse can best be explained through the bubble acceleration term in the Rayleigh-Plesset equation [22] ($\ddot{R}$):

$$\ddot{R} = -\frac{3\dot{R}^2}{2R} + \frac{1}{\rho_0 R}[p_g + p_v - \frac{2\sigma}{R} - \frac{4\mu\dot{R}}{R} - \rho_0 - p_s(t)] \quad (34)$$

$\dot{R}^2$ increases as the bubble collapses and hence the first term on the right becomes dominant in the equation [22]. Hence, $\ddot{R}$ can be approximated as:

$$\ddot{R} \approx -\frac{3\dot{R}^2}{2R} \quad (35)$$

The acceleration will be a negative number during this collapse and $\dot{R}$ will increase over time. Furthermore, the bubble wall will freely accelerate. This can also be shown using the principle of conservation of mass [22] (assuming $v_1 < v_2$):

$$4\pi R_1^2 v_1 = 4\pi R_2^2 v_2 \quad (36)$$

$$v_2 = (\frac{r_1}{r_2})^2 v_1 > v_1 \quad (37)$$

The contraction of the bubble causes the density inside the bubble (p_g) to increase. The density of the bubble becomes comparable to the liquid state outside of the bubble. The second term becomes dominant in the adjusted Rayleigh-Plesset equation and the bubble wall acceleration ($\ddot{R}$) turns into from a negative value to a positive value. Hence, the bubble collapse stops [22].

The resonance of the bubbles is dependent on the radii of the bubbles. This can be shown using the formula for the Minnaert resonance of a gaseous bubble in a liquid medium [26].

$$f_m = \frac{1}{2\pi r}(\frac{3\kappa}{\rho})^{\frac{1}{2}} \quad (38)$$

Where $\kappa = p_g * c_g^2$ with p_g being the density inside the bubble and c_g being the speed of sound in the bubble. The variable κ is calculated from the formula $\kappa = p_g * c_g^2$, where p_g is the density inside the bubble and c_g the speed of sound inside the bubble [26].

To determine the development of a radius across time, they used a Rayleigh-Plesset-type equation that, if solved, provides the radius over time R(t) [23]:

$$\rho(\ddot{R}R + \frac{3}{2}\dot{R}^2) = (P_0 + \frac{2\sigma}{R_0})(\frac{R_0}{R})^{3\kappa}(1 - \frac{3\kappa\dot{R}}{c}) - P_0 - P_A - \frac{2\sigma}{R} - \frac{4v\dot{R}}{R} \quad (39)$$

TABLE XIII: Symbols and their definitions of eq. (39)

Symbol	Definition	Symbol	Definition
$\dot{R}/\ddot{R}$	First/second time derivative	σ	
R	Time-dependant radius bubble	R_0	Initial bubble R
P_0	Local hydrodynamic pressure	v	
P_A	Acoustic pressure in channel	c	Speed of light
κ	Polytropic exponent gas bubble	ρ	Liquid density

The Rayleigh-Plesset equation used by Segers & Versluis has two additional terms that have not been included in the previous Rayleigh-Plesset equation. These are the assumptions of an ideal-gas law and some non-ideality in the reflection of the material. From table XIII the meaning of each respective symbol can be found. Segers & Versluis used several piezo actuators in their thickness mode (center frequencies 180kHz, 1MHz, 2MHz) to produce the ultrasound waves using sinusoidal waves at voltages 2.1V, 2.4V, and 2.7V. They used a maximum acoustic pressure amplitude P_A of 4.5kPa at the center of their channel. The shape of the P_A was a Gaussian shape [23]. Their chip was made out of PDMS since the PDMS-water interface had a significantly lower acoustic reflection rate (20% vs 95% in glass-water/silicon-water) [23]. Segers & Versluis also mention the importance of spacing between bubbles (d > 10R). If this condition is not adhered to, there is a larger chance of bubbles attracting and merging, which alters the resonance frequency of the bubble cluster significantly (and hence would impede the sorting process) [23]. Although the goal of their study was different, the findings of Segers & Versluis can be used as a valuable basis to start designing a bubble cavitating ultrasound piezo actuator.

The Rayleigh Collapse provides the mathematical foundations behind cavitating bubbles. Some predictions can also be made from this phenomenon. It can be seen that when the bubble wall collapses, it freely accelerates, and the velocity increases rapidly over time [22]. As demonstrated before, the velocity in a collapsing bubble increases as the radius decreases. From that point, it can be argued that a bubble with a larger initial radius can accumulate more force in its cavitation than a bubble with a smaller radius due to the increased distance from its center and free acceleration. To test this hypothesis, two different frequencies (and thus two

different bubble radii) will be determined and characterized for the experiments on LoC devices.

C. Lab-on-a-chip device

The design and production of the Lab-on-a-Chip devices has been done by Kleinsmit in their Master thesis on Design, fabrication, and validation of microreactors to study olivine carbonation in-operando with high-throughput [7]. Three reactors with different requirements have been designed. To optimise the reaction rate between olivine and CO_2 an increase in both temperature and pressure is required [7] [16]. The first reactor designed is the Constant Temperature microreactor that, as the name suggests, is a constant temperature throughout the reactor to facilitate the reaction between olivine and CO_2.The second reactor designed is the Temperature Gradient (TG) microreactor. This design relocates the reactor closer to the inlets to observe the effects of the gradual temperature changes on the olivine particles. The third and final reactor is named the Temperature and Pressure Gradient (TPG) microreactor. Temperature and pressure are key factors in carbonation rate. Hence, a reactor that allows the gradual increase of both factors can be interesting to observe [7]. This bachelor thesis uses the Constant Temperature (CT) microreactor. The main reason for this choice is that this thesis does need to meet the requirements imposed on the other two reactors. The CT microreactor is made of glass and sillicon. Two alternatives come to mind; PDMS and a glass-glass construction. PDMS is a versatile material that is relatively cost-effective to manufacture. The main reason why PDMS was not chosen was because of the pressure and temperature limits of PDMS. This did not align well with the goal of a high-pressure, high-temperature reactor, and therefore PDMS was not chosen as the manufacturing material [7]. Glass-glass and glass-silicon are better adept at handling (significantly) higher temperatures. The main reason for choosing glass-silicon instead of glass-glass was due to the bonding procedure. Anodic bonding provides the strongest bonds and cannot be done on glass [7]. Hence, the glass-silicon material provides both compatibility in terms of pressure and temperature requirements whilst also allowing for anodic bonding. The chip is manufactured in the MESA+ cleanroom at the University of Twente, where the silicon is etched using a five-step procedure [7]. The output of the fabrication process is a glass-silicon chip that consists of three inlets, two of which start at the beginning of the flow pattern and one that is added later to obtain the hypothesised precipitate $Mg(OH)_2$ [7]. Fluidic control is done through two high-pressure syringe pumps that allow for a controlled influx of each fluid under the desired pressure. The temperature and cooling are regulated by means of a PID-controlled cartridge heater and a thermoelectric cooler together with a heat sink. A standard microscope is used for optical inspection and filming [7]. These components and their models have been added to table XIV for completeness and can also be found in the thesis of Kleinsmit [7].

TABLE XIV: Equipment list for LoC device based on [7]

Use	**Model**
LoC device	CT microreactor
Syringe pumps	Cetoni neMESYS High Pressure
3 mL stainless steel syringe	–
Ball valves	Contiflow, Cetoni
Stainless steel tubing	Vici, 316SS, ID 0.04", OD 1/16"
Pressure sensors	Cetoni, $P_{max} = 200$ bar
PEEK connectors	IDEX, Microtight Fitting
Capillaries	Polymicro, ID/OD 100/360 μm
Epoxy glue	Araldite Rapid
Mid-pressure syringe pump	Cetoni Nemesys M
Microscope	Leica DMLM
PID controller	Red Lion, PXU21A20
Cartridge heater	RS PRO, 50 W, 220 VAC
Solid state relay	TE Connectivity, SSRT-240D25
Thermocouple	Type K
Copper block	2×2×4 cm
Heat sink	Dow Corning 340
Mechanical relay	RS PRO, 450-0330
Cooling fluid	G11, $C\&C$ Automotive
Thermoelectric cooler	Thermorack 401

D. Additional results

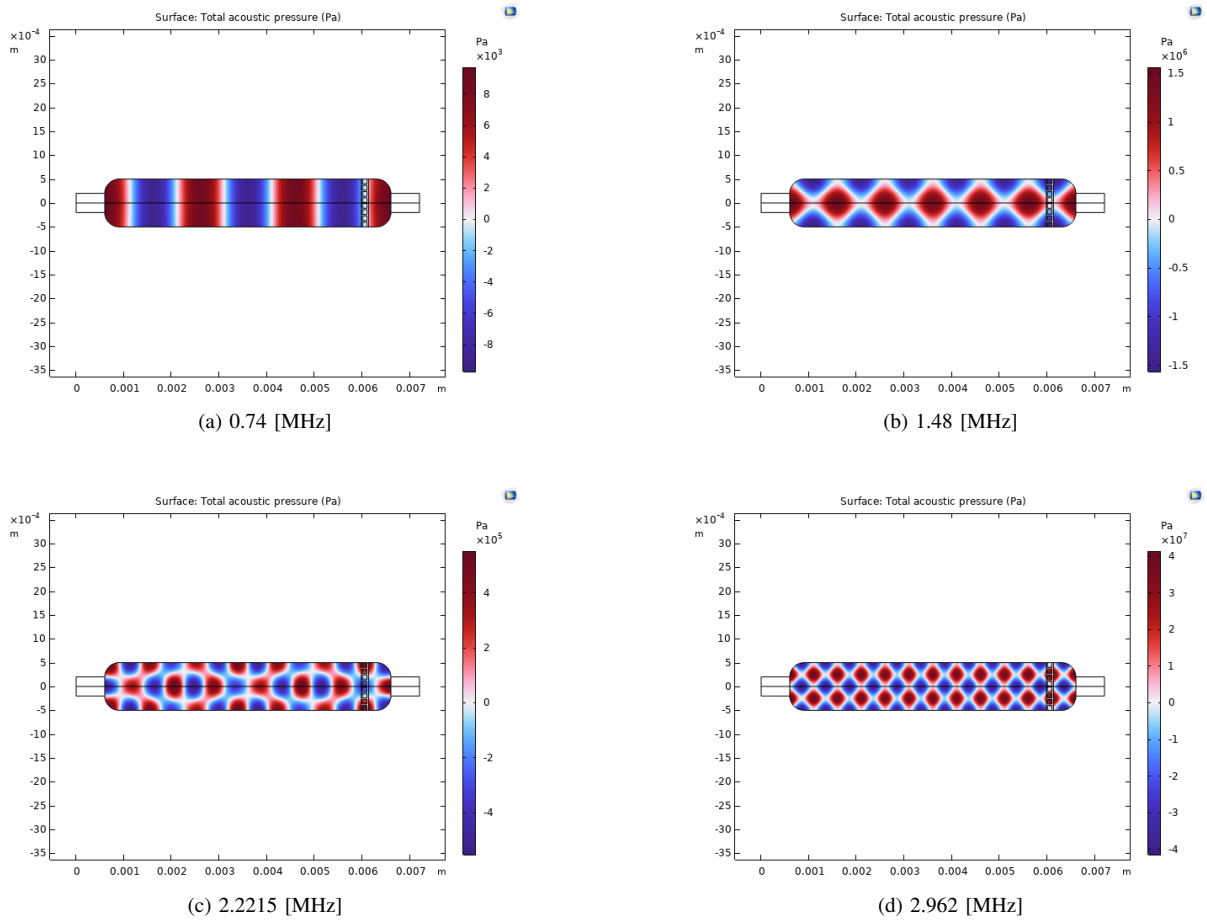

(a) 0.74 [MHz]

(b) 1.48 [MHz]

(c) 2.2215 [MHz]

(d) 2.962 [MHz]

Fig. 19: Acoustic pressure plots for N = 1, 2, 3, 4 at 10 [nm] actuation

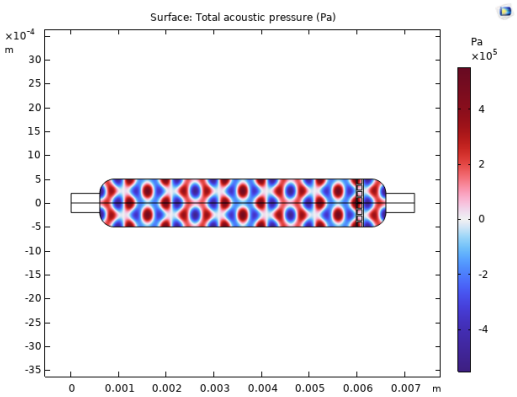

(a) 3.7025 [MHz]

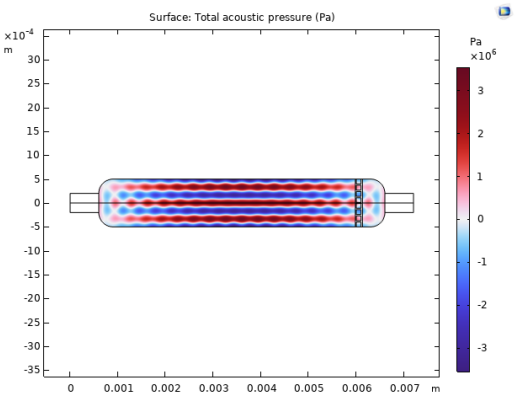

(b) 4.443 [MHz]

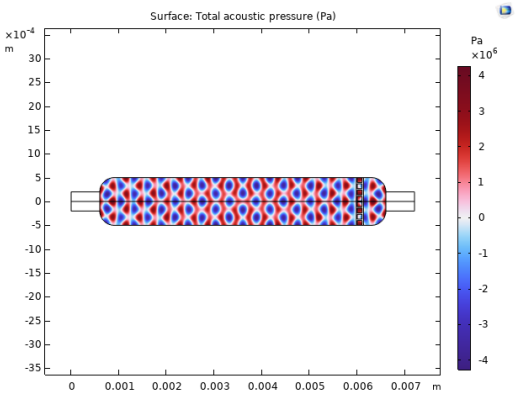

(c) 5.1835 [MHz]

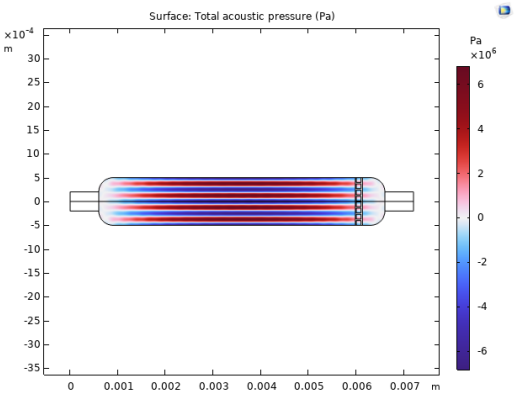

(d) 5.924 [MHz]

Fig. 20: Acoustic pressure plots for N = 5, 6, 7, 8 at 10 [nm] actuation

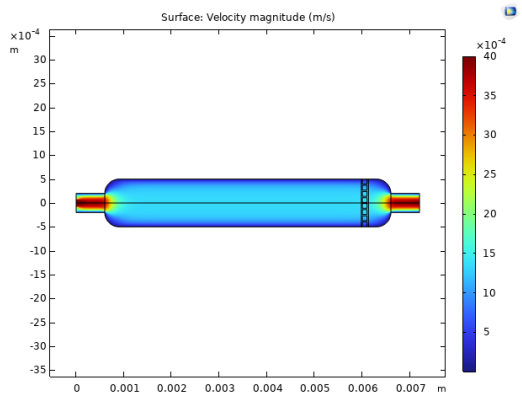

(a) 0.74 [MHz]

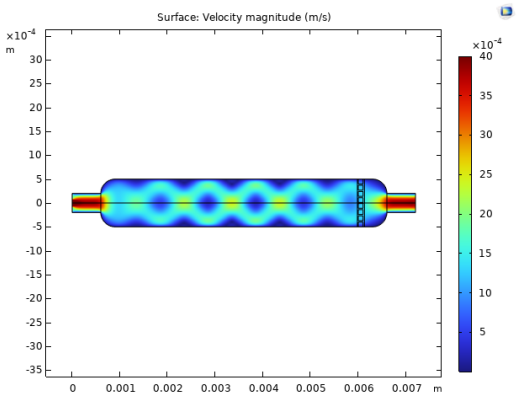

(b) 1.48 [MHz]

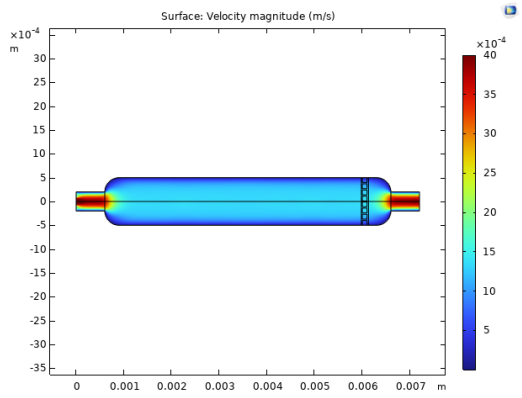

(c) 2.2215 [MHz]

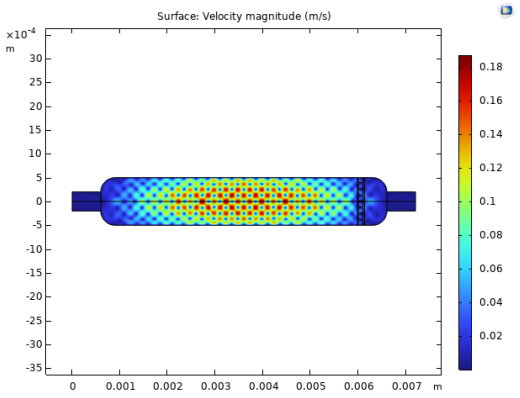

(d) 2.962 [MHz]

Fig. 21: Velocity magnitude plots for N = 1, 2, 3, 4 at 10 [nm] actuation

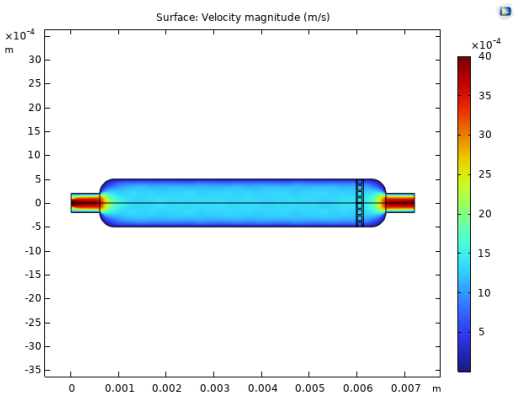

(a) 3.7025 [MHz]

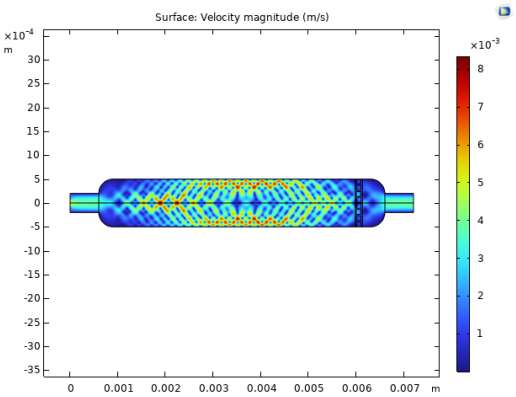

(b) 4.443 [MHz]

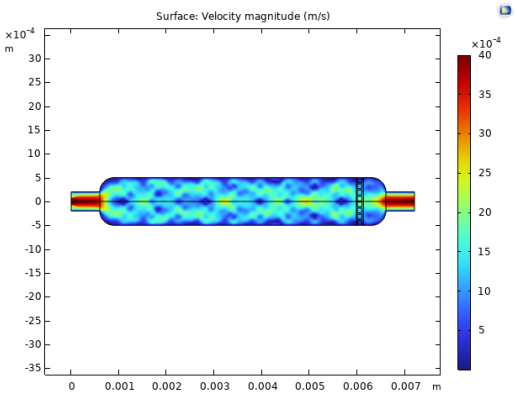

(c) 5.1835 [MHz]

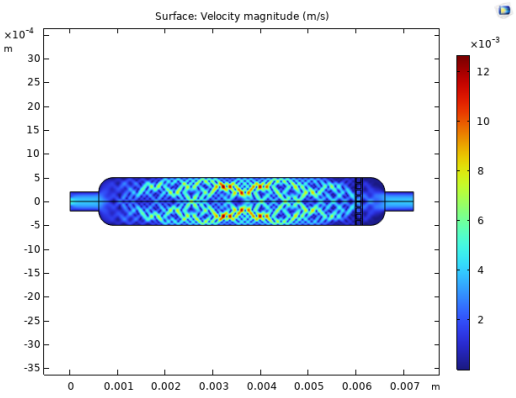

(d) 5.924 [MHz]

Fig. 22: Velocity magnitude plots for N = 5, 6, 7, 8 at 10 [nm] actuation

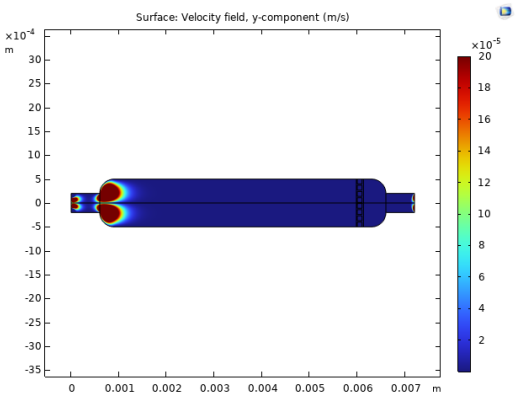

(a) 0.74 [MHz]

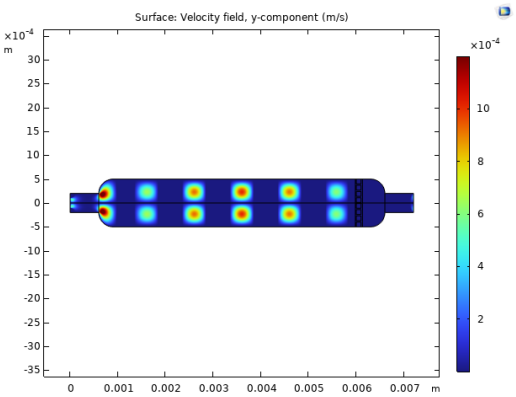

(b) 1.48 [MHz]

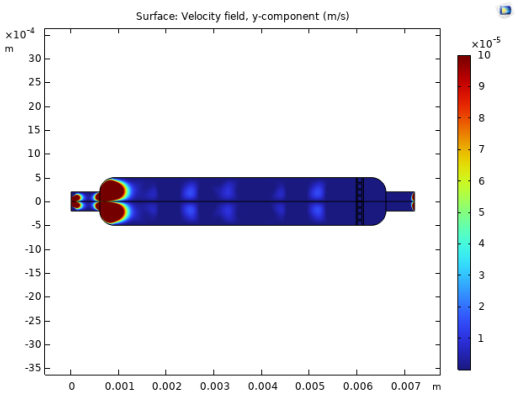

(c) 2.2215 [MHz]

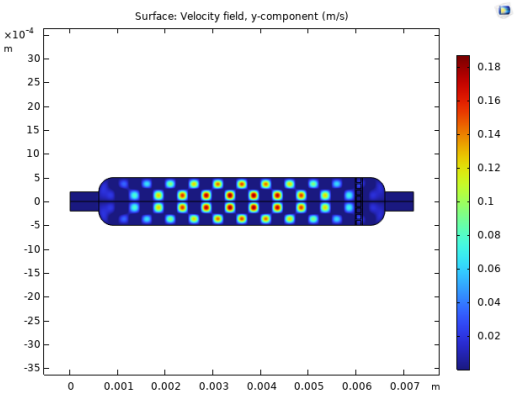

(d) 2.962 [MHz]

Fig. 23: Velocity y component for N = 1, 2, 3, 4 at 10 [nm] actuation

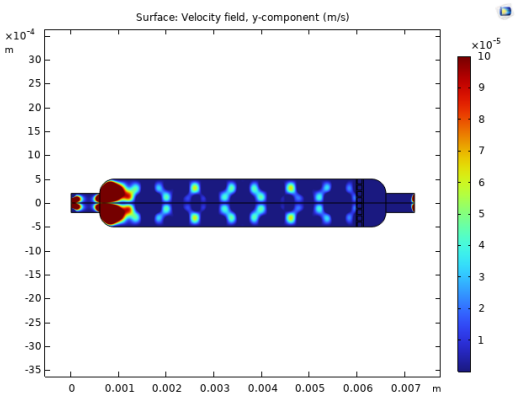

(a) 3.7025 [MHz]

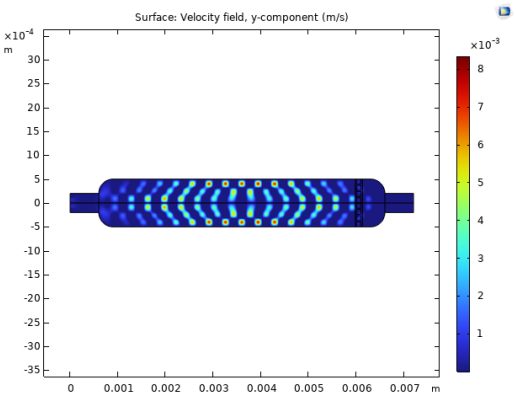

(b) 4.443 [MHz]

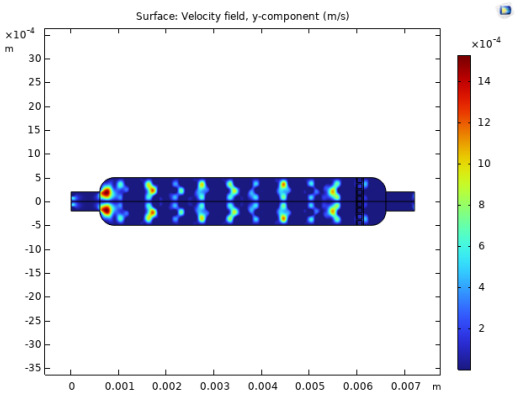

(c) 5.1835 [MHz]

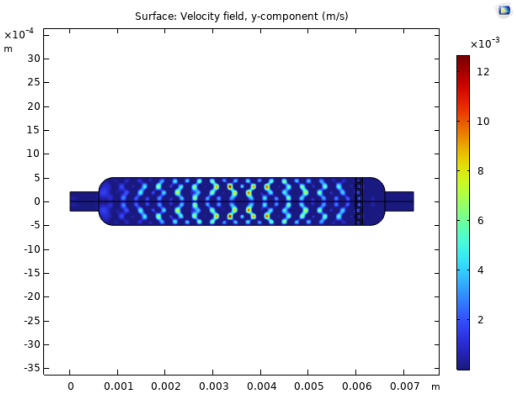

(d) 5.924 [MHz]

Fig. 24: Velocity y component for N = 5, 6, 7, 8 at 10 [nm] actuation

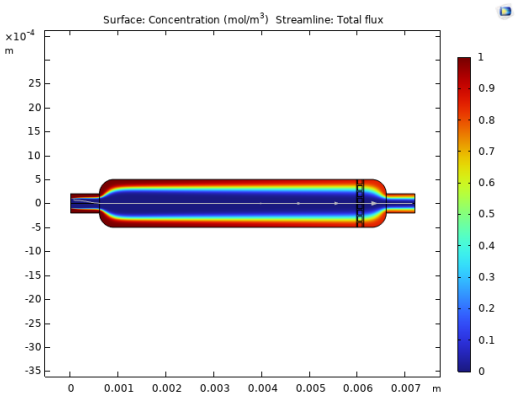

(a) 0.74 [MHz]

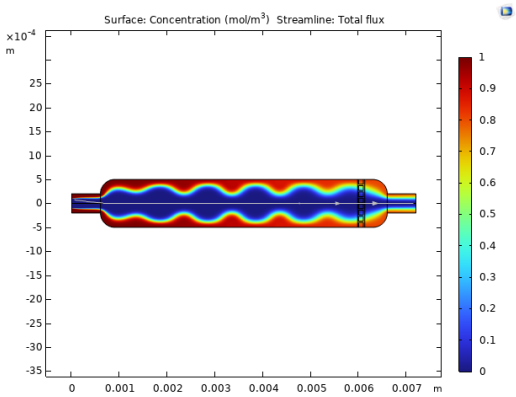

(b) 1.48 [MHz]

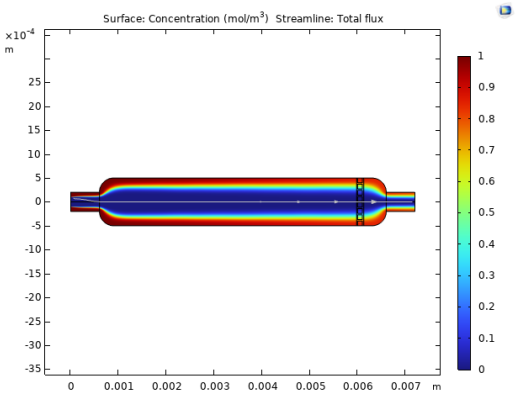

(c) 2.2215 [MHz]

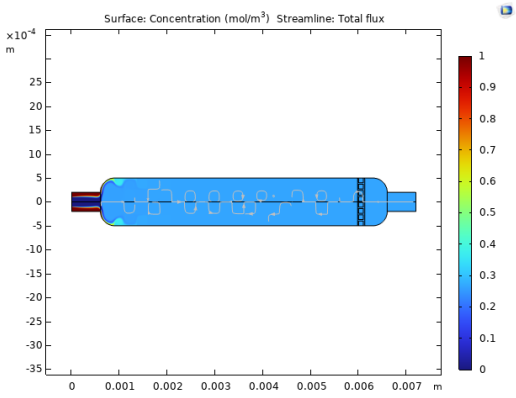

(d) 2.962 [MHz]

Fig. 25: Concentration gradient plots for N = 1, 2, 3, 4 at 10 [nm] actuation

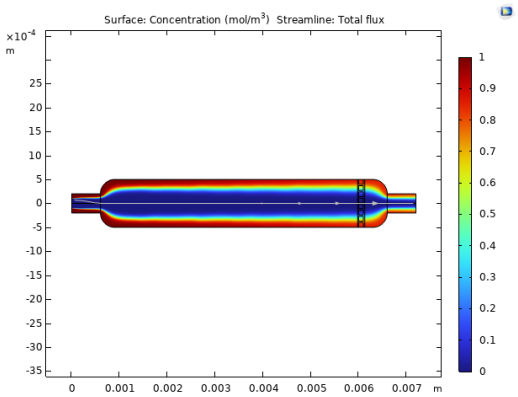

(a) 3.7025 [MHz]

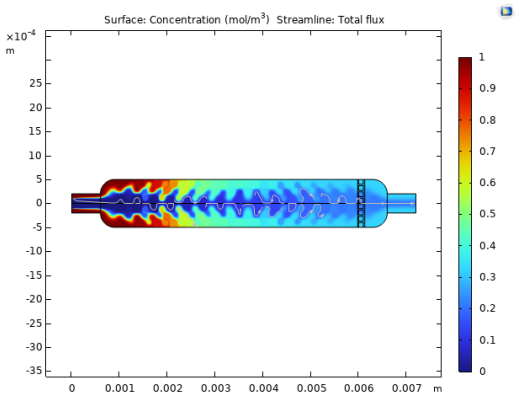

(b) 4.443 [MHz]

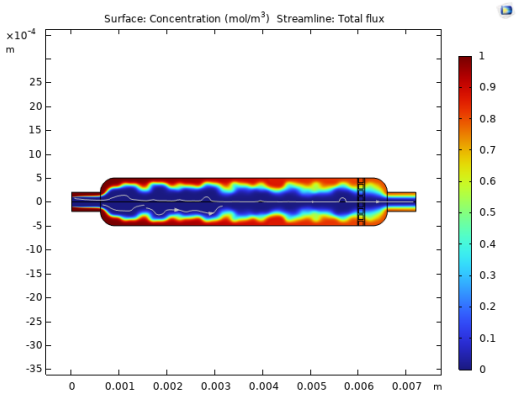

(c) 5.1835 [MHz]

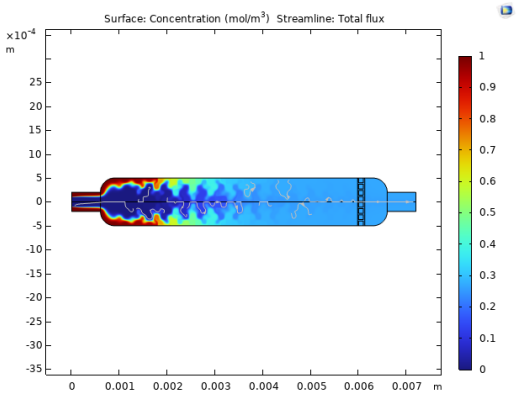

(d) 5.924 [MHz]

Fig. 26: Concentration gradient plots for N = 5, 6, 7, 8 at 10 [nm] actuation

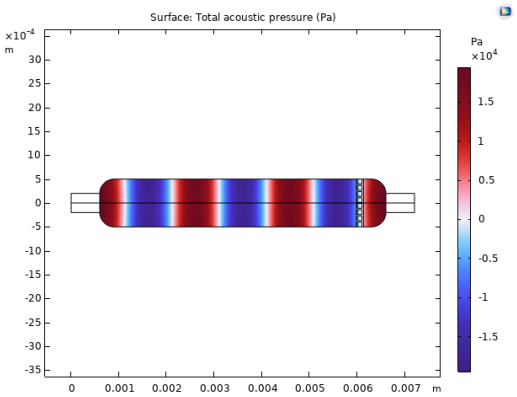

(a) 0.74 [MHz]

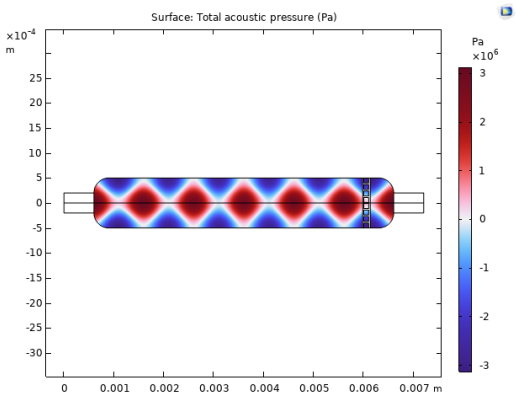

(b) 1.48 [MHz]

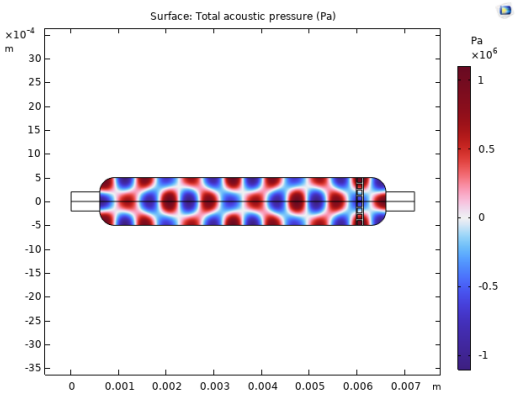

(c) 2.2215 [MHz]

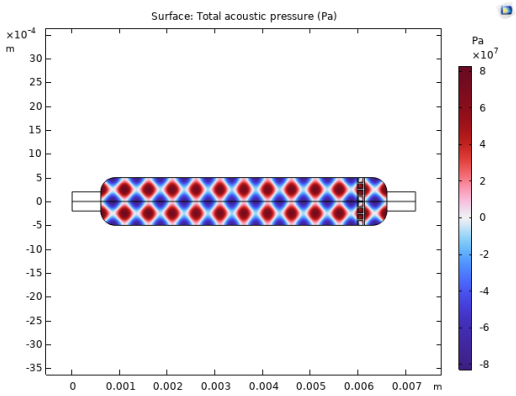

(d) 2.962 [MHz]

Fig. 27: Acoustic pressure plots for N = 1, 2, 3, 4 at 20 [nm] actuation

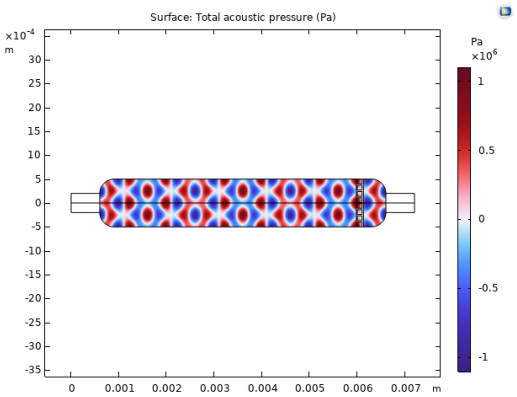

(a) 3.7025 [MHz]

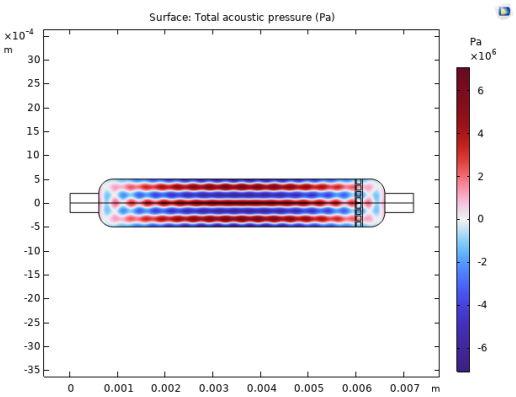

(b) 4.443 [MHz]

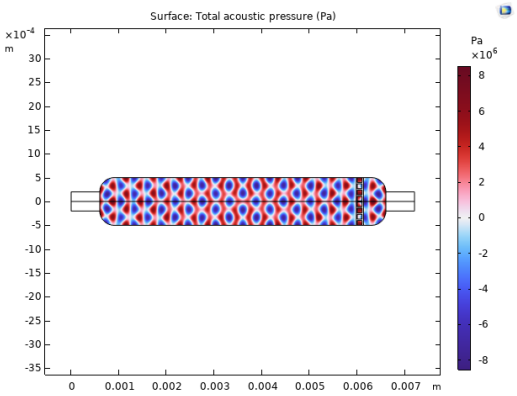

(c) 5.1835 [MHz]

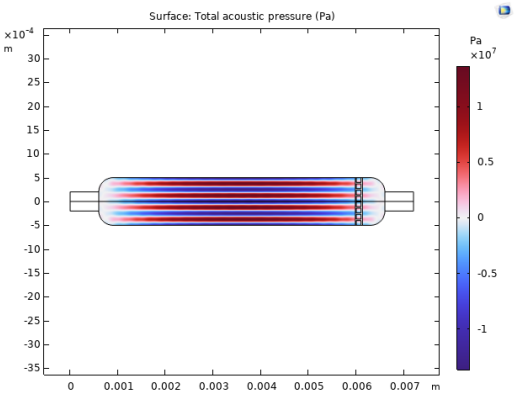

(d) 5.924 [MHz]

Fig. 28: Acoustic pressure plots for N = 5, 6, 7, 8 at 20 [nm] actuation

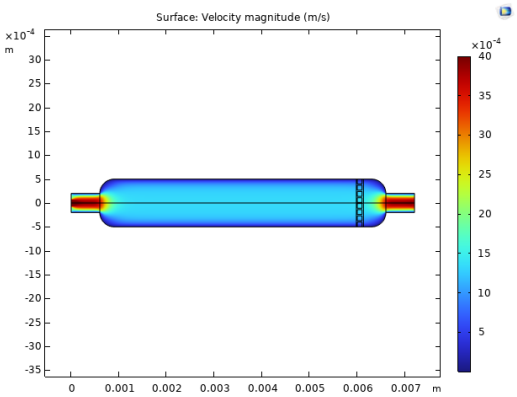

(a) 0.74 [MHz]

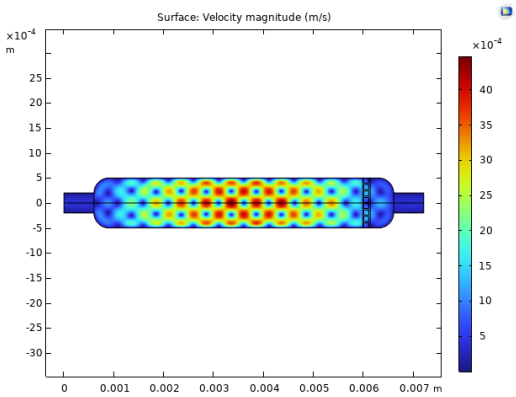

(b) 1.48 [MHz]

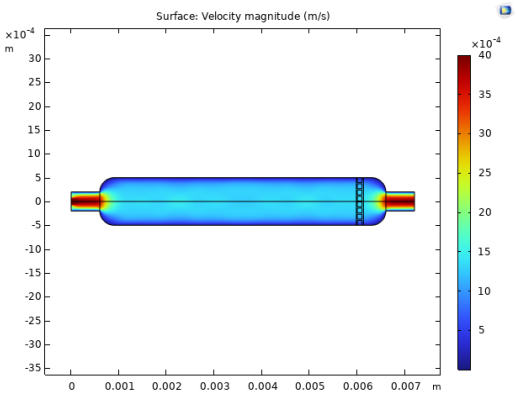

(c) 2.2215 [MHz]

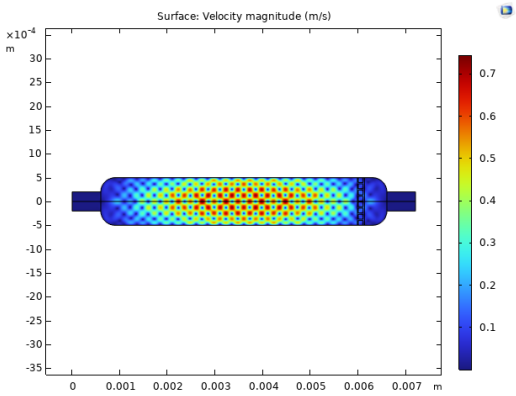

(d) 2.962 [MHz]

Fig. 29: Velocity magnitude plots for N = 1, 2, 3, 4 at 20 [nm] actuation

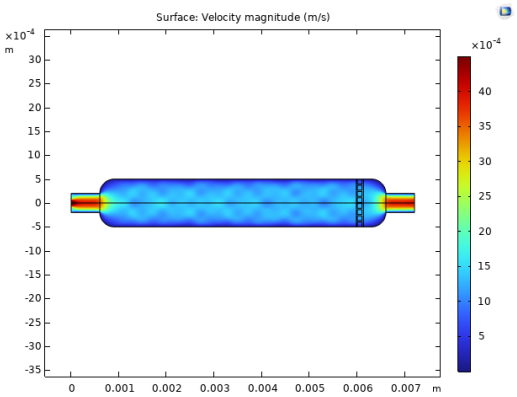

(a) 3.7025 [MHz]

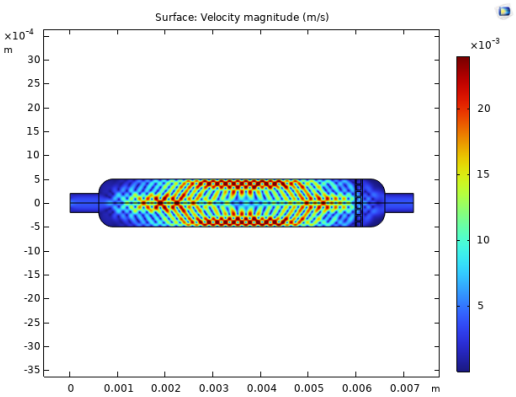

(b) 4.443 [MHz]

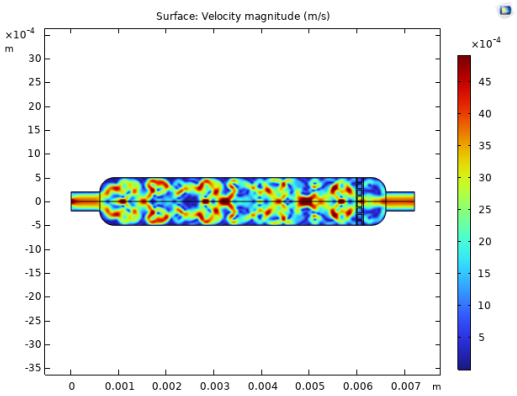

(c) 5.1835 [MHz]

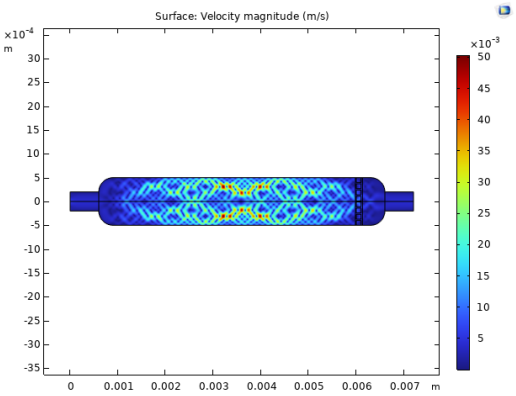

(d) 5.924 [MHz]

Fig. 30: Velocity magnitude plots for N = 5, 6, 7, 8 at 20 [nm] actuation

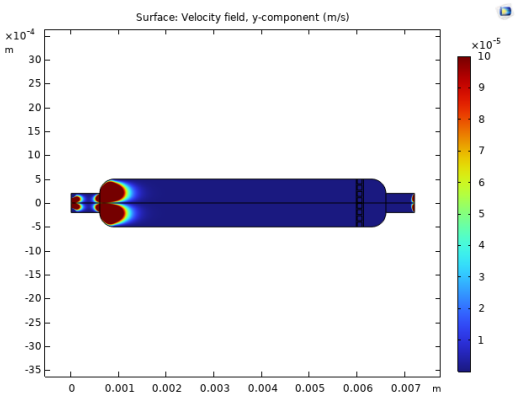

(a) 0.74 [MHz]

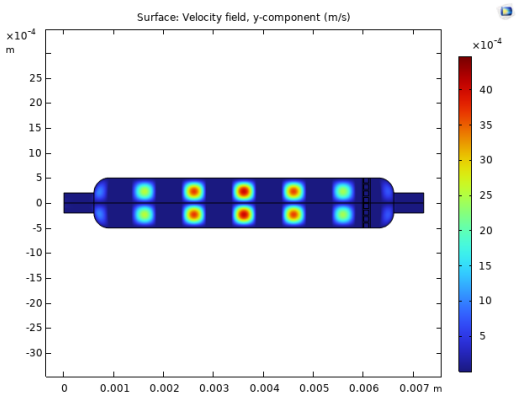

(b) 1.48 [MHz]

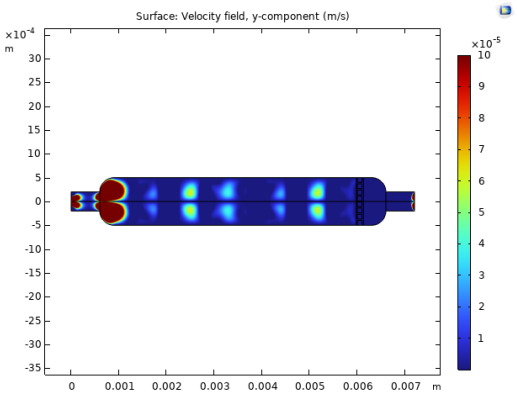

(c) 2.2215 [MHz]

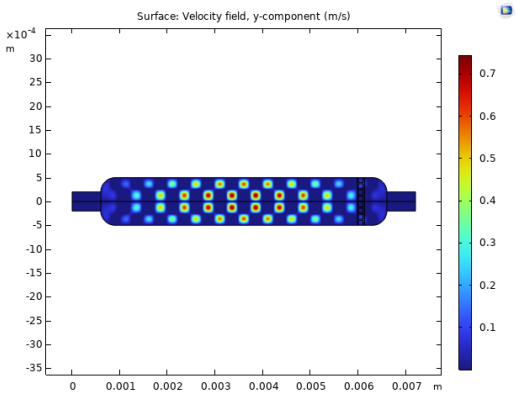

(d) 2.962 [MHz]

Fig. 31: Velocity y component for N = 1, 2, 3, 4 at 20 [nm] actuation

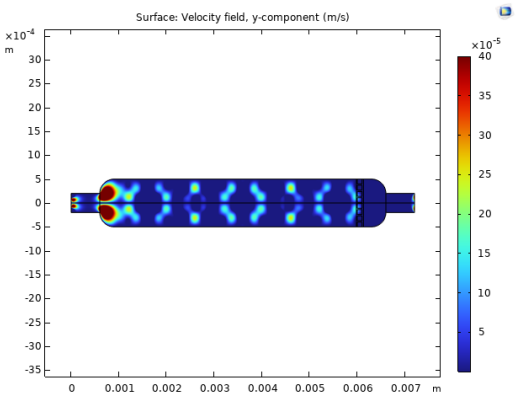

(a) 3.7025 [MHz]

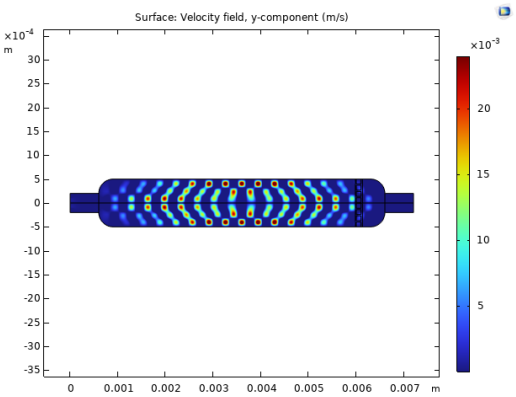

(b) 4.443 [MHz]

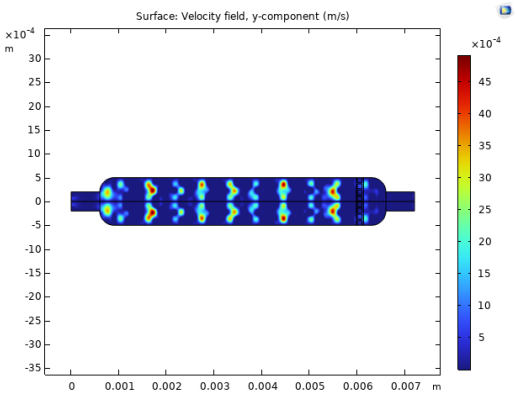

(c) 5.1835 [MHz]

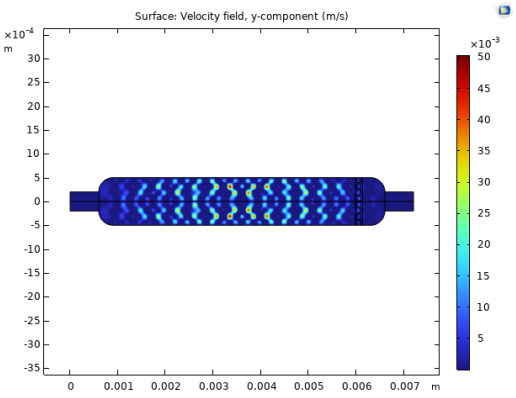

(d) 5.924 [MHz]

Fig. 32: Velocity y component for N = 5, 6, 7, 8 at 20 [nm] actuation

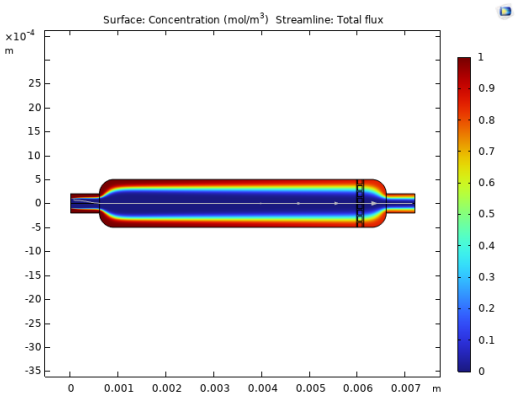

(a) 0.74 [MHz]

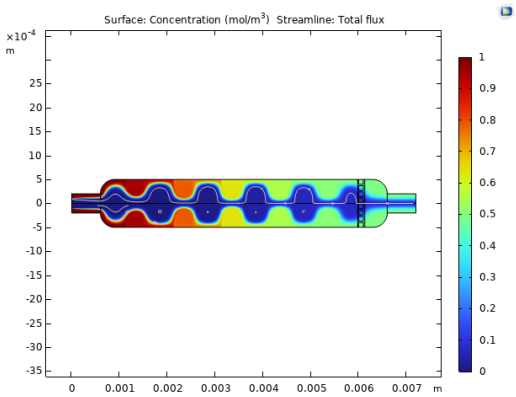

(b) 1.48 [MHz]

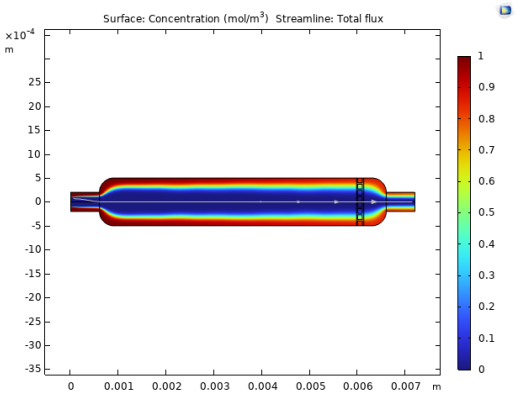

(c) 2.2215 [MHz]

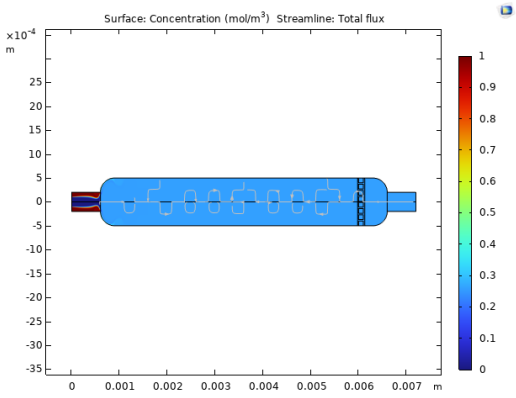

(d) 2.962 [MHz]

Fig. 33: Concentration gradient plots for N = 1, 2, 3, 4 at 10 [nm] actuation

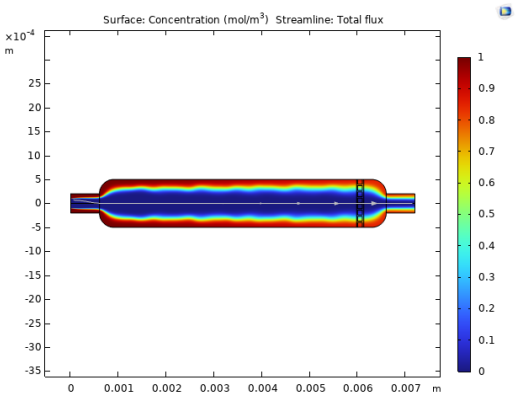

(a) 3.7025 [MHz]

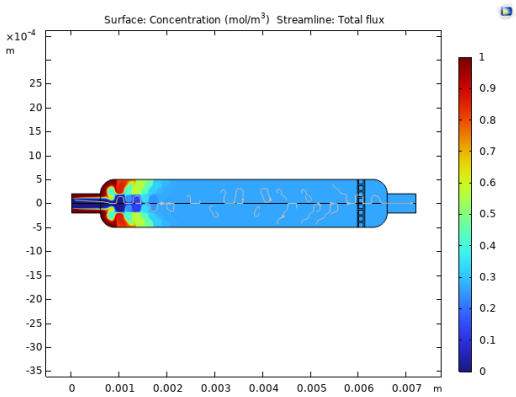

(b) 4.443 [MHz]

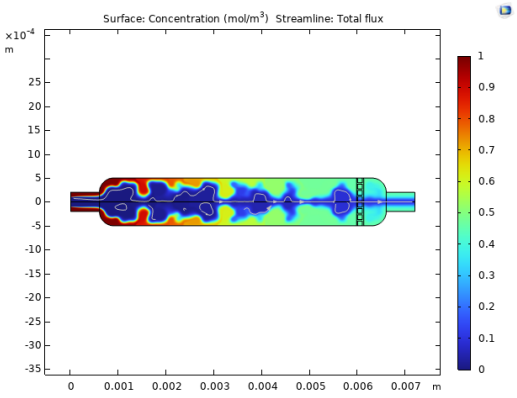

(c) 5.1835 [MHz]

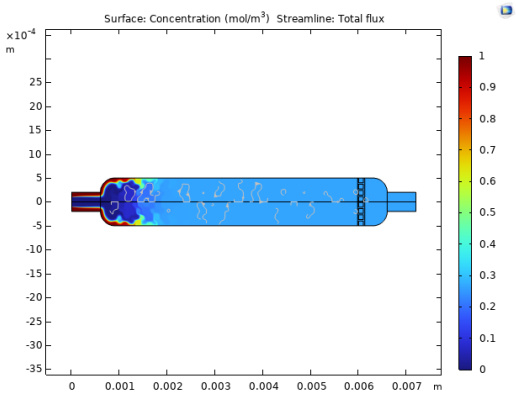

(d) 5.924 [MHz]

Fig. 34: Concentration gradient plots for N = 5, 6, 7, 8 at 20 [nm] actuation

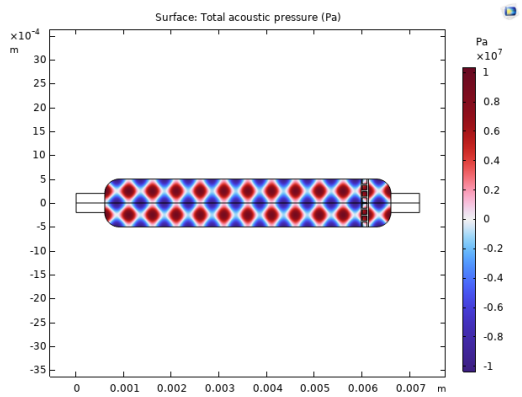

(a) Acoustic pressure

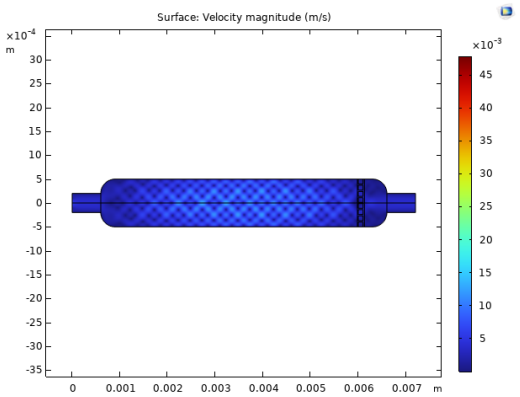

(b) Velocity magnitude

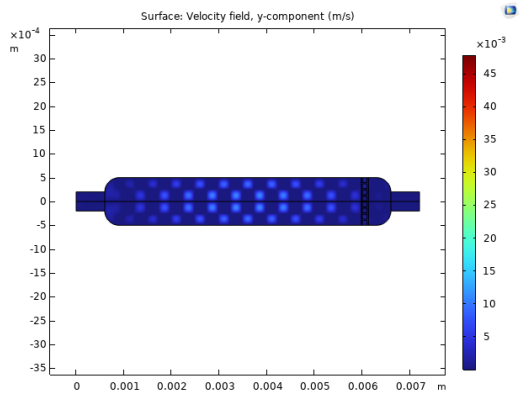

(c) Velocity y component

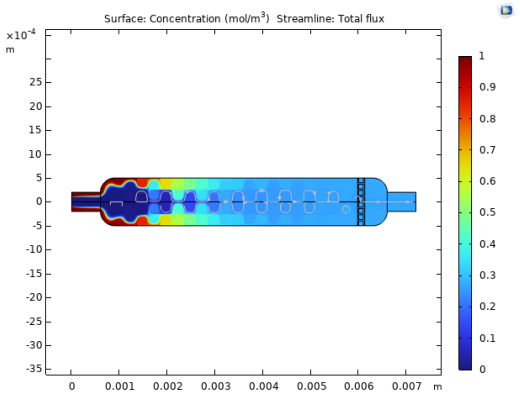

(d) Concentration gradient

Fig. 35: Acoustic pressure, velocity magnitude, velocity y component and concentration gradient plots with 2.5 [nm] actuation at 2.962 [MHz]

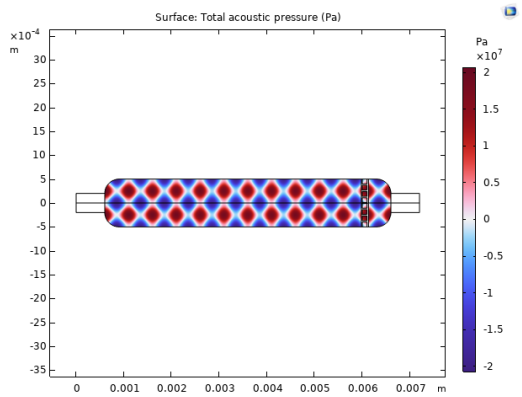

(a) Acoustic pressure

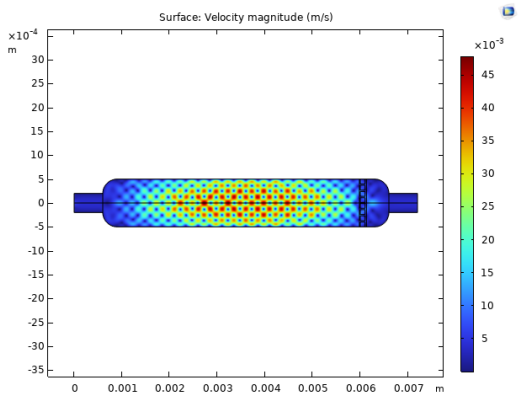

(b) Velocity magnitude

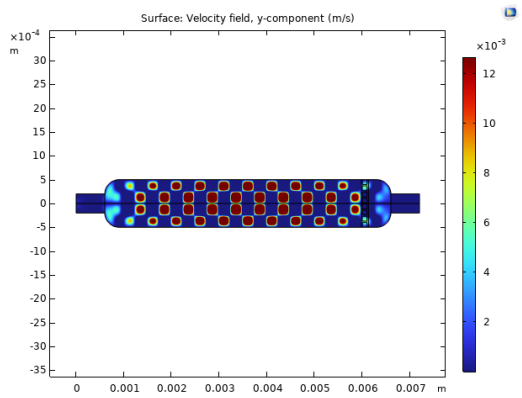

(c) Velocity y component

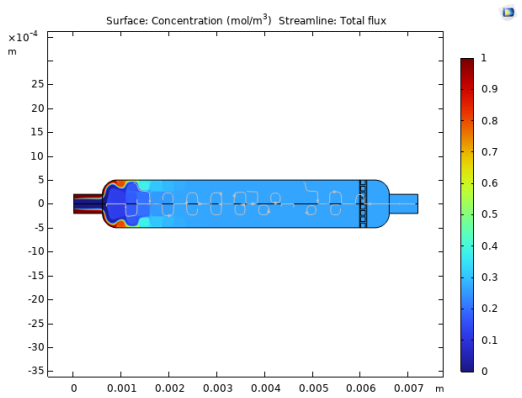

(d) Concentration gradient

Fig. 36: Acoustic pressure, velocity magnitude, velocity y component and concentration gradient plots with 5 [nm] actuation at 2.962 [MHz]

E. Plan of action

1) Abstract: ***Abstract*—This plan of action describes a study of the effects of how ultrasonic actuation phenomena—such as microjetting, streaming, and cavitation—affect the formation and disruption of the passivation layer on olivine in a liquid CO_2 mixture. Four different piezoceramic bulk resonators (740, 550, 360, 169 (kHz)) were designed based on the correlation between the size of the microchannel (1mm) and the medium(s) (CO_2, H_2O, fluorescend dye) inside the microchannel. Using these bulk resonators, three distinct experiments were done to test and validate the effects of ultrasonic actuation on micron-level channels on so called lab-on-a-chip devices (LoC).**

2) Background: Human activities have been climate change's major driver in the 21st century [1]. Global warming through the output of greenhouse gasses has caused the global surface temperature to rise by 1.1 degrees Celsius compared to preindustrial temperature levels. More extreme weather phenomena have been observed throughout the last decade, affecting much of the human population. These extreme weather events cause food and water insecurity, ecosystem damage, a disease-susceptible environment, and many other potential crises[1]. Various solutions have been or are currently developed to combat these greenhouse gas emissions of the past, present, and future. One of the more known greenhouse gasses is CO_2. It is by far the most common greenhouse gas and it is estimated to comprise approximately 80% of the greenhouse gasses mix (79.7% in 2022 in the U.S [2] and 80.6% in 2024 in the EU [3]). CO_2 will be the gas focussed on in this study. There are two main catagories for reducing the greenhouse gas (GHG) problem. One is through reducing the emissions that are outputted to the atmosphere. This can be done either through a reduction of comsumption or through innovations that reduce the output of GHG's of the goods and/or services. The other method of combating the GHG problem is by reducing the GHGs that are already present in the air. This is what we call carbon sequestration. Carbon sequestration focuses on capturing and storing CO_2 in the earth, flora, and through reaction products with rocks for a long period [4] [5]. Trees are the most commonly known form of CO_2 sequestration. This also means that carbon sequestration is natural and man-made [4]. Other forms of carbon sequestration can be through direct air capture, other vegitation and through (ultra-mafic/mafic) rocks. This research will focus on carbon sequestration. Currently, CO_2 is emitted through various actors, one of the largest being the concrete industry. They are estimated to emit around 8% of the world emissions [8] [9]. To reduce the carbon footprint of the process, some organizations have started to capture the CO_2 from the emission process. Although this is a step in the right direction, there is a potential to sequester the CO_2 through carbonation with ultra-mafic and mafic rocks [10]. Olivine, a mafic rock, is used as a CO_2 sequestration method. It can be deployed in a natural setting (e.g. on beaches) and in a stirring setup with liquid CO_2 to enhance the reaction between CO_2 and olivine [10]. However, the current process is heavy-wearing in which stirring materials and containers frequently require replacement and the reaction process is relatively slow [11].

A potential avenue for development to enhance the reaction process is within Lab-on-a-Chip research (LoC). Lab-on-a-chips can be seen as mini-reactors with a large variety of experimental options. The pressure can be heightend, the flowrate can be adjusted, the temperature can be fluctuated and external tools such as lasers or ultrasonic waves can be used to influence the LoC environment. Kleinsmit developed such a reactor that allows the reaction between olivine particles and CO_2 to happen at a high temperature and under a high pressure [7]. The preliminary results indicated a significant initial reaction rate. However, this slowed down at a later stage due to the passivation layers on the partially reacted olivine particles [7]. Ultrasound was suggested as an avenue for development to address these passivation layers around olivine particles. Hence, the purpose of this thesis is to investigate the response of the passivation layers of olivine in a LoC environment by applying an ultrasonic wave onto the LoC device. The mineral storage of CO_2 seems to be one of the most permanent solutions to the modern day climate change problem [13]. The longevity of this storage compared to other forms of carbon storage such as through vegitation and soils is incomparable. Mineral rocks are able to store CO_2 for millions of years where vegitation and soils are limited to decades, centuries or millenia. The storage potential of these mineral rocks is nearly infinite and potentially valuable byproducts can be created through the reactions with CO_2.

However, the natural process of mineral carbonation is not fast enough to keep up with or compensate for the emissions of yesterday, today and tomorrow. To have a chance of reaching the climate goals set up by organisation like the European Union, several challenges of mineral carbonation need to be addressed. Among these are; the slow mineral-fluid interaction, the impact of the mining required to excavate these materials, in some cases energy-intesive pre-treatment, the high energy costs required to hasten the reaction kinetics and the overall economic viability of mineral carbonation [13] [14] [15]. These are challenges that have to be solved in order for mineral carbonation to be seen as an appropriate and effective, partial, solution to climate change. The world "partial" is stressed here as CO_2 sequestration should not take away from the effort to reduce emissions. CO_2 sequestration should focus on the alleviating the effects that are currently present and aid the sectors that find difficulty in transforming towards CO_2 neutrality.

There are differences between the methods of mineral carbonation. Olajire makes a distinction between three different archetypes of mineral carbonation. In-situ, ex-situ and other forms [15] [14] [13]. In-situ mineral the original place, and in the case of mineral carbonation this is generally underground. The carbon is injected underground and the environmental conditions are optimised to facilitate the natural reaction process. Ex-situ is the more commonly known idea within mineral carbonation technologies (MCT's) and refers to process of treating the CO_2-mineral reaction in an industrial process setting [15] [14] [13]. The heading "other" is used by Olajire

for two different MCT's; passive and biomineralisation [15]. Passive refers to the natural process of mineral carbonation [15]. Biomineralisation refers to the use of living organisms to aid in precipitation processes. It should not be seen as an alternative to the geological storage of carbon but rather as a solution in specific scenarios [15].

One of the materials proposed for mineral carbonation is olivine. Olivine, consisting out of the chemical mix of magnesium iron sillicate, are one of the most common minerals on earth. Olivines can be found in ultramafic and mafic igneous rocks and are abudently found in the earth's rock mantle. Its abundance is one of the advantages in the considerations for CO_2 sequestration. Its chemical formula is $(Mg, Fe)_2SiO_4$. The reactivity between olivine and CO_2 has been demonstrated in the literature [16]. Garcia et al. found in their experiments with supercritical CO_2 (150 C°) and 150 bar) that $57\% \pm 2\%$ of the CO_2 was sequestered, with its main reaction product being magnesite and in low concerations amorphous silica [16]. Olivine has been suggested as a method for CO_2 sequestration in various papers. Several of those papers describe the the uses of olivine in coastal zones [17] [18] [19]. These tropical zones would induce increased weathering which would speed up the reaction between olivine and CO_2. Similar approaches have been proposed for olivine in combination with coastal locations. The increased alkilinity in the water would increase the CO_2 uptake from sea-air interaction. However, more reseach is required to estimate the risks and costs paired with introducing olivine to the sea. These include ecological effects, economical viability, (potential) secondary reactions and dissolution reactivity [19] [18]. Bearat et al. have shown that the reaction between olivine and CO_2 produces a reaction-inhibiting layer that is largely composed out of silica [20]. This is more generally known as a passivation layer and has been observed in several papers on the mineral carbonation of olivine [10] [20] [21]. The passivation layers of olivine inhibit the reaction between the CO_2 and olivine particles which causes the reaction to slow down.

One of the proposed options to break these passivation layers in olivine and thus assist the carbonation process of olivine is through acoustic cavitation. Ultrasound-intensified carbon sequestration makes use of frequencies above the human hearing range (>20kHz) to cavitate microbubbles that are actuated (through resonance) by ultrasonic waves. The process of acoustic cavitation makes use of microbubbles in water that are actuated by ultrasonic waves. These microbubbles expand and shrink in size due to linear or non-linear resonance [22]. The bubble pulsates for a large range of bubble radii and can violently collapse if the acoustic amplitude is significant enough to incite strong pulsations [22]. This phenomenon occurs on the premise that the chosen bubble radius matches the range of bubble radii required for resonance at the chosen acoustic amplitude. A comparable experiment was done in the paper of Segers & Versluis on acoustic bubble sorting for ultrasound contrast agent enrichment [23]. In their paper, Segers & Versluis provide a bubble sorting theory that uses ultrasound as its sorting method through bubble resonance. They added an ultrasound piezo perpendicular to their LoC flow setup to elevate the y-level of resonating bubbles. Segers & Versluis recommended a traveling wave due to its wavelength being independent of channel dimensions, hence allowing optimization without altering the chip design [23].

A visualization of the effects of ultrasonic-induced cavitation is important to understand how ultrasonic-induced cavitation can enhance the mineral carbonation process. This is shown in Wagterveld et al.'s paper, where they used acoustic cavitation on suspended calcite crystals intending to visualize the acoustic cavitation effects [24]. Wagterveld et al. differentiate between cluster and stream cavitation. Cluster cavitation refers to the formation and clustering of cavitation bubbles, that then collapse together, generating a strong local impulse. Wagterveld et al. observed that the force generated by these cluster cavitations was able to cause three different forms of impact; attrition, disruption of aggregates, and deagglomeration [24]. The second form of cavitation bubbles encountered by Wagterveld et al. was streamer cavitation. This refers to the formation and clustering of cavitation bubbles in the form of strings. The collapse of this string releases localized impulses across a larger surface area and hence generates less impact on one place in the volume (as compared to cluster cavitation). Due to its decrease in localized impact, streamer cavitations were observed to only cause deagglomeration [24]. Another finding of Wagterveld et al. was regarding circular indentations in the formed calcite when they investigated it with a scanning electron microscope (SEM). Wagterveld et al. argued that this was likely due to shockwave-induced jet impingements (high-velocity fluids directed at a surface) [24]. Wagterveld et al.'s article on visualizing the effects of acoustic cavitation on minerals provides a hopeful outlook on removing or decaying the passivation layer on olivine.

Acoustic cavitation has been proposed and used for applications in fields such as surface finishing, agri-food, non-invasive medical monitoring, pathogen deactivation and drug delivery [25] [26] [27] [28]. Another research area for acoustic cavitation is the mineral carbonation field. Santos et al. investigated how ultrasound can assist the process of mineral carbonation [11]. The aim was to use stainless steel slags to sequester CO_2 and reduce their alkalinity. The study evaluated the differences between mechanical mixing and mechanical mixing aided by an ultrasound probe. Evaluations also showed a difference in results due to the positioning of the ultrasound. These experiments were conducted in intervals of four hours and at a consistent temperature of 50 degrees Celsius [11]. The results showed that a continuous ultrasound-intensified mixing process improved the reaction the most. The periodic ultrasound-intensified mixing process also showed improvements when compared to the baseline of solely mechanical mixing. Nevertheless, the economic aspect in terms of energy costs was an important limitation of the study. Santos et al. determined that with the energy costs and the energy mix at that time, it was not viable to capture more CO_2 than was emitted through the ultrasound-intensified process [11]. A new avenue of this could be the use of green energy to slope off the

carbon consumption of the process [11]. The removal and/or decaying of the passivation layer of olivine is what this thesis will be about. So far, the process of using ultrasonic cavitation to decay the passivation layer of olivine has not yet been visualized in detail. A gap in the literature remains as to how ultrasound impacts Olvine particles in a LoC environment. There are two main effects that are likely to be observed when ultrasound is applied to a (micro) fluidic device. The generation and/or cavitation of bubbles and the generation of streaming inside the channel. This bachelor thesis will focus on creating an ultrasonic actuator setup on a LoC device that aims to generate streaming and microjetting on olivine particles inside the LoC to visualize the process and impact.

Throughout this review of the literature, it has become evident that tackling the olivine passivation layer could bring great benefits when it is used later for CO_2 sequestration [10]. Ultrasound is one of the promising options for the decay of the passivation layer of olivine, as has been demonstrated in other similar cases [11] [24]. Santos et al. [11] have shown that ultrasonic acoustic actuation appears to improve the reaction rate; however, this process has not yet been visualized and has not been done on olivine particles. Wagterveld et al. [24] show the potential effects of acoustic cavitation and actuation (its standalone effect) using suspended calcites crystals, and this provides a hopeful outlook for the effects of ultrasonic actuation on the passivation layer of olivine. The introduction to bubble resonance theory given in the article by Segers & Versluis provides valuable information as to how to design such a set-up [23]. The main differences lie in the applications (mixing vs. sorting) and the materials inside the LoC environment (liquid and olivine particles vs. pure liquid).

To summarise, the purpose of this study has been to investigate how ultrasound and its acoustic actuation properties can be used to decay the passivation layer found around olivine particles. This thesis will focus on designing and building an ultrasonic actuation set-up that is used on a LoC device to generate streaming, microjetting, and cavitating bubbles. The hypothesis is that the ultrasonic actuation can induce significant improvements in the decay of the passivation layers of the olivine particles in the LoC device. The main research question is as follows:

- To what extent do ultrasonic actuation phenomena—such as microjetting, streaming, and cavitation—affect the formation and disruption of the passivation layer on olivine in a liquid CO_2 mixture, and how do these effects correlate with visible signs of improved carbonation?

3) Analysis: The choice of glass-silicon as a material has an impact on how ultrasound is used on the chip. The reflection coefficient of glass-silicon is high and thus allows (almost) no traveling waves to go through the glass interface. To allow ultrasound to enter the channel, standing waves should be generated in the channel. This can be done by vibrating the chip with a piezoceramic resonator. The deciding factor in choosing the operating frequency for a standing wave is the width of the channel. The chosen design (CT microreactor) uses a 1mm wide channel in the reactor room. Thus, for a standing wave to form in the channel, its wavelength should be at most twice the size of its width. Turning wavelength into frequency using eq. (40) provides a frequency of approximately 740kHz for a single standing wave to form in the channel considering a medium of water at 20 degrees Celsius (v = 1481 m/s). Similarly, for liquid CO_2 at 20 degrees (and 57.291 bar) the speed of sound is 337.65 m/s [29]. Following eq. (40) this leads to a frequency of approximately 169 kHz. The mixture of CO_2 and water (H_2O) changes the speed of sound based on the composition of the mixture, the applied pressure, and the temperature. Each piezo can be driven on a range of frequencies surrounding its resonance frequency. Hence, to bridge the "gap" between the two extremes (only H_2O or only liquid CO_2), two different piezos are necessary. This allows for different compositions of H_2O vs CO_2 to be tested. Two additional piezos at 360 kHz and 550 kHz allow for a dynamic range of frequencies to be examined.

These standing waves will have two antinodes, at the edges of the channel, and one node in the middle of the channel (see fig. 37). With this frequency, the piezo-dimenions can be determined. From the website of CTS Ferroperm Piezoceramics [52], it can be seen that piezoceramic plate resonators are known to be versatile and excel in unidirectional displacement. Since the chip of this experiment requires such specifications, it is best to opt for the shape of a square. Thus, the final specifications for the piezoceramic resonators are plate-shaped and are based on the dimensions of the channel in which they should operate.

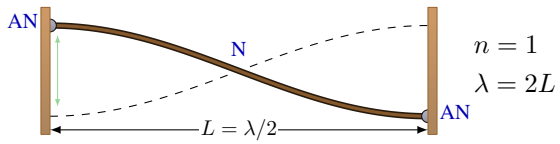

Fig. 37: Standing wave, double free

The resonance frequency of a bulk square piezoceramic resonator is calculated through its respective dimensions. A bulk resonator generates its resonance frequency through deformation of the piezoceramic material. The formula for calculating the frequency of a wave is as follows:

$$f = \frac{c}{\lambda} \tag{40}$$

The resonance frequency of a wave is based on the constructive interference of waves. For resonance to occur, the round-trip phase must match the starting phase. When not aligned, the summation of the two waves would result in a suboptimal output compared to the resonance frequency production. The resonance frequencies of a square resonator can be calculated by integrating the phenomenon described above into eq. (40). For resonance to occur, the phase of a round-trip wave has to equal the phase of a starting wave. Thus, λ should fit the dimension of the resonator (d) [30]. For a round-trip, a value of 2d is the minimal value for resonance. The minimal resonance

value (2d) is called the fundamental frequency. Any positive number can expand this to find higher harmonics, as can be seen in the formula below:

$$f_r = \frac{Nc}{2d} \tag{41}$$

Here, N is any positive integer number, c is the speed of a wave, and d is the length of any side of a square resonator. A similar calculation can be made for a circular piezoceramic resonator, taking into account the spherical symmetry. To calculate the measurements for the required piezoceramic resonators, the formula is rewritten as follows:

$$d = \frac{Nc}{2f_r} \tag{42}$$

In piezoceramic material (lead zirconium titanate, PZT), the propagation speed of the wave is between 3500 m/s and 4500 m/s [31]. The value for c used in the calculations is 4000 m/s. The thickness of the 740kHz resonator thus becomes approximately 2.7mm. The height and width also provide resonance frequencies. For practical purposes, these values are chosen to be 5mm (with a estimated resonance frequency of 400kHz). The measurements of the bulk square resonator for the water-based experiments is 5mm x 5mm height by width and its thickness is 2.5mm. Similarly, the thickness of the bulk square resonator for experiments based on liquid CO_2 is approximately 11.8mm. This provides another piezo with a thickeness of 11.8mm and the same 5mm x 5mm height by width as the previous piezo. The respective thicknesses of the piezos at 360 kHz and 550 kHz would be approximately 5.6mm and 3.6mm. To avoid interference in these piezos, larger widths and heights are chosen so that the respective resonance frequencies of the thicknesses are not tampered with. The final measurements would be 5.6mm x 10mm x 10mm and 3.6mm x 8mm x 8mm.

4) Methodology: This section details the materials, workflow, settings, and experiments relevant to this thesis. The design choices for the piezoceramic resonator have been justified in the previous section. To generate a standing wave in the 1 mm reactor channel of the LoC device, the frequency must be tuned to match the properties of the medium within the microchannel. Based on this requirement, four piezoceramic resonators were designed at frequencies of 740 kHz, 550 kHz, 360 kHz, and 169 kHz following eq. (40). These frequencies correspond to resonator dimensions of 2.7×5×5mm, 3.6×8×8 mm, 5.5×10×10mm, and 11.8×5×5mm, respectively (see eq. (42)). Each piezoceramic plate resonator requires a driving voltage to achieve its resonance behaviour. The higher the voltage, the higher the acoustic pressure amplitude. The frequency should match the intended operating frequency with considerations for slight deviations in the resonance frequency (e.g. 700-800 kHz for the 740 kHz resonator). The frequency range comes from the fact that the non-idealities from the piezoceramic resonator are likely to cause a slight shift in the resonance frequency due to e.g. material imperfections. In table XV and table XVI the components required to make the piezoceramic plate resonator and the LoC device work can be found.

TABLE XV: Equipment list piezoceramic resonators

Use	Model
Piezoceramic resonator 740 kHz	Plate 2.7x5x5 (mm)
Piezoceramic resonator 550 kHz	Plate 3.6x5x5 (mm)
Piezoceramic resonator 360 kHz	Plate 5.6x5x5 (mm)
Piezoceramic resonator 169 kHz	Plate 11.8x5x5 (mm)
Function generator	Agilent 33120A
Amplifier	-
Coupling circuit/transformer	-
Oscilloscope	Rhode and Schwartz RTB2002
Coax cables	-
Coax cable splitter	-
Glue	-
Copper wire	-
Soldering station	-
RLC meter	Rohde and Schwarz/Hameg HM8118

TABLE XVI: Equipment list LoC device based on [7]

Use	Model
LoC device	CT microreactor
Syringe pumps	Cetoni neMESYS High Pressure
3mL stainless steel syringe	-
Ball valves	Contiflow, Cetoni
Stainless steel tubing	Vici, 316SS, ID 0.04", OD 1/16"
Pressure sensors	Cetoni, Pmax = 200 bar
PEEK connectors	IDEX, Microtight Fitting
Capillaries	Polymicro, ID/OD 100/360 μm
Epoxy glue	Araldite Rapid
Mid-pressure syringe pump	Cetoni Nemesys M
Microscope	Leica DMLM
PID controller	Red Lion, PXU21A20
Cartridge heater	RS PRO, 50 W, 220 VAC
Solid state relay	TE Connectivity, SSRT-240D25
Thermocouple	Type K
Copper block	2x2x4 (cm)
Heat sink	Dow Corning 340
Mechanical relay	RS PRO, 450-0330
Cooling fluid	G11, $C\&C$ Automotive
Thermoelectric cooler	Thermorack 401

The piezo is driven by a voltage to generate displacements (vibrations) at (and around) its resonance frequency. To actuate this voltage, a function generator is needed. This generator needs to be able to output frequencies up to 850kHz to accommodate a range of possible resonance frequencies. Furthermore, an increase in amplitude results in an increase in the acoustic amplitude following eq. (43), where V is the voltage and p is the acoustic pressure.

$$V \propto p \tag{43}$$

Precise voltage - acoustic amplitude relations require calibration of the piezos. This is possible using a calibrated hydrophone in a bath of water. The calibrated hydrophone has a known voltage - acoustic amplitude relation, and from there, the piezos can be calibrated. A more brute-force method can be applied in the experiments by increasing the voltage and observing the response of the piezoceramic resonator (the acoustic amplitude) to see what happens. Aside from this, the response in the medium inside the microchannel can also be

observed. E.g. for experiment 1, this would result in observing sudden significant diffusion between the fluorescend dye and water.

The piezoceramic resonator needs testing to verify its frequency response and input impedance. This is necessary to ensure that there are no undesired effect from or towards the function generator. Depending on the required voltage, a high-voltage amplifier might be necessary to realise the intended response from the piezo. An impedance analyser can be used to analyse the input impedance of the piezo. Most function generators have a relatively low output impedance (50 Ω). The input impedance of the piezo should not be too high or too low. The maximum power transfer comes from following Thevenin's maximum power transfer theorem, which states $Z_{source} = Z_{load}$. In the case of a high input impedance from the piezo ($>> 50\Omega$) most of the voltage will drop across the piezo. Following eq. (44), if the impedance of the piezo is too high, the power transfer is low. To combat this, a high-voltage amplifier can be connected to the system to increase the power transfer to the piezo.

$$P = \frac{V_{piezo}^2}{Z_{piezo}} \tag{44}$$

A low input impedance of the piezo ($<< 50\Omega$) results in a large voltage drop across the internal resistance of the function generator (50Ω). This comes from the voltage division between the internal output impedance of the function generator and the input impedance of the piezo. This also decreases the voltage transferred to the piezo following eq. (44) since V_{piezo} is significantly reduced.

There are several ways to match the input impedance of the piezo to the output impedance of the function generator. If the piezo shows capactive behaviour from the impedance analysis (or by measuring it with and RLC meter) its impedance can be matched using an LC matching circuit. The configuration of this circuit depends on the real and imaginary impedance values of the piezo at resonance. Another approach uses a transformer that matches that can step up or step down the impedance that the function generator sees depending on the configuration of coils in the transformer. A less efficient but possible alternative for stepping down the input impedance of the piezo is a resistive divider, but this is undesirable due to the power losses from dissipation.

The design and production of the Lab-on-a-Chip devices has been done by Kleinsmit in their Master thesis on Design, fabrication, and validation of microreactors to study olivine carbonation in-operando with high-throughput [7]. Three reactors with different requirements have been designed. To optimise the reaction rate between olivine and CO_2 an increase in both temperature and pressure is required [7] [16]. The first reactor designed is the Constant Temperature microreactor that, as the name suggests, is a constant temperature throughout the reactor to facilitate the reaction between olivine and CO_2.The second reactor designed is the Temperature Gradient (TG) microreactor. This design relocates the reactor closer to the inlets to observe the effects of the gradual temperature changes on the olivine particles. The third and final reactor is named the Temperature and Pressure Gradient (TPG) microreactor. Temperature and pressure are key factors in carbonation rate. Hence, a reactor that allows the gradual increase of both factors can be interesting to observe [7]. This bachelor thesis uses the Constant Temperature (CT) microreactor. The main reason for this choice is that this thesis does need to meet the requirements imposed on the other two reactors. The CT microreactor is made of glass and sillicon. Two alternatives come to mind; PDMS and a glass-glass construction. PDMS is a versatile material that is relatively cost-effective to manufacture. The main reason why PDMS was not chosen was because of the pressure and temperature limits of PDMS. This did not align well with the goal of a high-pressure, high-temperature reactor, and therefore PDMS was not chosen as the manufacturing material [7]. Glass-glass and glass-silicon are better adept at handling (significantly) higher temperatures. The main reason for choosing glass-silicon instead of glass-glass was due to the bonding procedure. Anodic bonding provides the strongest bonds and cannot be done on glass [7]. Hence, the glass-silicon material provides both compatibility in terms of pressure and temperature requirements whilst also allowing for anodic bonding. The chip is manufactured in the MESA+ cleanroom at the University of Twente, where the silicon is etched using a five-step procedure [7]. The output of the fabrication process is a glass-silicon chip that consists of three inlets, two of which start at the beginning of the flow pattern and one that is added later to obtain the hypothesised precipitate $Mg(OH)_2$ [7]. Fluidic control is done through two high-pressure syringe pumps that allow for a controlled influx of each fluid under the desired pressure. The temperature and cooling are regulated by means of a PID-controlled cartridge heater and a thermoelectric cooler together with a heat sink. A standard microscope is used for optical inspection and filming [7]. These components and their models have been added to table XVI for completeness and can also be found in the thesis of Kleinsmit [7].

The piezoceramic plate resonator will be glued to the LoC device. To avoid issues such as overheating or local extremes in pressure, the piezo will be turned on in short sprints of several milliseconds. The duration of time and voltage largely determine the response of the piezo. In the experiments, these two variables will be closely tuned to find the desired response. The specific desired response will vary per experiment, but the overall goal is to increase the energy (e.g. pressure, temperature, motion) in the microchannel. The workflow of the experimental section is described chronologically in table XVII. Furthermore, a electrical circuit diagram of the setup has been provided in fig. 38.

Before any experiment is conducted, the setup will be clearly labelled with appropriate voltage range warnings. The system will always be voltage-free before any physical contact is made with the piezo or surrounding components. When appropriate, the student will wear insulating gloves to minimize the risk of accidental conduction. Additionally, the student will

TABLE XVII: Workflow of the experiments

Task	Check
Determine f_r of piezos	✓
Determine impedance piezos	✓
Determine coupling circuit	✓
Determine Voltage–Acoustic amplitude relation	✓
Add high-voltage amplifier (if necessary)	✓
Test-run chip without piezo	✓
Glue piezo on chip	✓
Test response piezo on chip	✓
Test and document experiment 1	✓
Test and document experiment 2	✓
Test and document experiment 3	✓

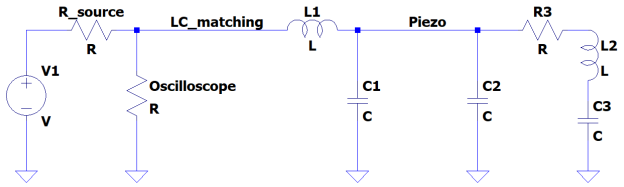

Fig. 38: Electrical circuit diagram of the setup using a low-pass LC matching circuit and a simulated piezoceramic resonator

always inform another BIOS group member before starting any experiment involving voltages, to ensure that no work is done alone in the lab. Experiments are conducted in short bursts (milliseconds) to reduce thermal or mechanical stress on the piezo element. After each trial, the function generator is turned off immediately to halt all piezo activity. The input voltage is constantly monitored using an oscilloscope. In case of any unexpected signal deviations, the experiment is halted immediately, and the student steps away from the setup only after the function generator is safely powered down. All microfluidic channels are visually inspected for leaks before any voltage is applied. Electrical components are placed at a maximum safe distance from fluidic components to minimize any risk of short-circuiting or leakage-induced conduction. Additionally, open fluidic systems are strictly prohibited in the vicinity of high-voltage components. Only sealed or properly enclosed microfluidic devices will be used in conjunction with electrical equipment.

Three experiments will be examined during this study. The first experiment will test how well the laminar flow of water and the fluorescend dye mix during the actuation of the piezoceramic resonator. Normally, the laminar flow will not be disturbed largely as only contact areas will experience some diffusion. The goal of ultrasonic actuation is to induce pressure nodes and microjets/streams that induce (significantly) more diffusion. The degree of mixing will be analyzed using a high-resolution microscope with qualitative measurements. A fluorescent dye will be introduced into one of the inlet streams, and the diffusion pattern will be captured using the camera (Flir) attached to the microscope. The piezoceramic resonator will be activated at voltage levels of 5V 10V and 20V to evaluate the correlation between acoustic energy and mixing behavior. From there, the voltage will be empirically tuned to find the best diffusion response. The hypothesis of experiment 1 is as follows: Ultrasonic actuation generates a standing wave in the microchannel that generates a pressure node, which together with microjetting induces significantly more diffusion and disturbs the laminar flow in the microchannel of the LoC device. The second experiment studies the effect of introducing microbubbles into a laminar flow with only water at 20 degrees Celsius and low pressures (<500kPa). These low pressure conditions make sure the microbubbles do not collapse immediatly. The microbubbles will be generated using the bubble maker inside the BIOS general lab. The radius of the microbubbles determines their resonance frequency using the Minnaert formula eq. (38). Ultrasonic actuation with a high acoustic amplitude is able to induce strong oscillations into the microbubbles, leading to bubble collapse. This is more commonly known as cavitation. The bubble releases significant energy locally upon collapse. This generates temperature and pressure differences locally. First, bubbles with radii based on the theoretical Minnaert resonance frequency are used to validate the cavitation response inside the microchannel. If necessary, the bubble radii can be adjusted for a better response to the applied frequency. The acoustic pressure amplitude will be controlled through the voltage applied. The voltage will be varied from 0-20V to observe different cavitation intensities. If necessary, a high-voltage amplifier can be added to increase the power transfer to the piezo. An important consideration is the possibility of bubble clustering or bubble coalescence. Bubble clustering essentially allows bubbles to stick closely together in groups. Bubble coalescence is the process of two bubbles merging into one. Each situation significantly alters the resonance frequency of the bubbles. To avoid these situations, Segers & Versluis used a protocol that the distance, d, between two bubbles in the microchannel should be greater than 10 times the radius of the bubble [23]. To summarise, the aim of the experiment is to visualise the collapse of bubbles in a LoC device through ultrasonic actuation. The hypothesis of experiment 2 is as follows: The ultrasonic actuation of microbubbles in a laminar water flow will show the collapse of microbubbles and the generation of microjets and streaming effects through locally generated pressure differences. The third experiment examines the effects of ultrasonic actuation on a mixture of water and liquid CO_2 and the effects on the carbonation process of olivine particles in the reactor. The olivine sample used in this experiment has an average particle size of 50-250 μm and fits into the reactors [7]. The experiment will be conducted in a supercritical CO_2 environment at a pressure of >73 bar [7] and a temperature of 100 degrees Celsius. Kleinsmit experienced difficulties with the driving force of gaseos to liquid CO_2 due to an equilibrium in pressure (57 bar) at room temperature. To avoid these issues, Kleinsmit cooled the syringe to ensure a lower equilibrium pressure of 45 bar [7]. This method was able to successfully fill the reactor with liquid CO_2 and will also be used for this experiment. It is important to note that the proposed conditions are not optimal conditions for the carbonation of olivine [7] [16]. These conditions were

chosen to ensure safety and to allow for local variations in pressure and temperature. Ultrasonic actuation will be applied at frequencies of 169, 360 and 550 kHz to induce microjetting and streaming effects. This is expected to mechanically disrupt the passivation layer formed on the olivine surface, allowing fresh mineral exposure and enhancing CO_2 diffusion with the newly exposed olivine surfaces. The goal of the third experiment is to investigate whether ultrasonic actuation can affect the carbonation process of olivine. The hypothesis for experiment 3 is as follows: Ultrasonic actuation generates local pressure and temperature differences through the generation of pressure nodes, microjetting, and streaming. These effects are hypothesised to be helpful in increasing the yield of the olivine carbonation process CO_2 by increasing the reactive surface area of olivine particles. The results can be observed by inspecting the particle morphology of the olivine remnants with ultrasound compared to the control condition without ultrasound.